arXiv:1304.6875v1 [astro-ph.HE] 25 Apr 2013

A Massive Pulsar in a Compact Relativistic Binary*

John Antoniadis,[1] † Paulo C. C. Freire,[1] Norbert Wex,[1] Thomas M. Tauris,[2,1]
Ryan S. Lynch,[3] Marten H. van Kerkwijk,[4] Michael Kramer,[1,5] Cees Bassa,[5]
Vik S. Dhillon,[6] Thomas Driebe,[7] Jason W. T. Hessels,[8,9] Victoria M. Kaspi,[3]
Vladislav I. Kondratiev,[8,10] Norbert Langer,[2] Thomas R. Marsh,[11]
Maura A. McLaughlin,[12] Timothy T. Pennucci,[13] Scott M. Ransom,[14]
Ingrid H. Stairs,[15] Joeri van Leeuwen,[8,9]
Joris P. W. Verbiest,[1] David G. Whelan,[13]

[1]Max-Planck-Institut für Radioastronomie, Auf dem Hügel 69, 53121 Bonn, Germany
[2]Argelander Institut für Astronomie, Auf dem Hügel 71, 53121 Bonn, Germany
[3]Department of Physics, McGill University, 3600 University Street, Montreal, QC H3A 2T8, Canada
[4]Department of Astronomy and Astrophysics, University of Toronto,
50 St. George Street, Toronto, ON M5S 3H4, Canada
[5]Jodrell Bank Centre for Astrophysics, The University of Manchester,
Alan Turing Building, Manchester, M13 9PL, UK
[6]Department of Physics & Astronomy, University of Sheffield, Sheffield, S3 7RH, UK
[7]Deutsches Zentrum für Luft- und Raumfahrt e.V. (DLR),
Raumfahrtmanagement, Königswinterer Str. 522–524, 53227 Bonn, Germany
[8]ASTRON, the Netherlands Institute for Radio Astronomy,
Postbus 2, 7990 AA Dwingeloo, The Netherlands
[9]Astronomical Institute "Anton Pannekoek", University of Amsterdam,
Science Park 904, 1098 XH Amsterdam, The Netherlands
[10]Astro Space Center of the Lebedev Physical Institute,
Profsoyuznaya str. 84/32, Moscow 117997, Russia
[11]Department of Physics, University of Warwick, Coventry, CV4 7AL, UK
[12]Department of Physics, West Virginia University, 111 White Hall, Morgantown, WV 26506, USA
[13]Department of Astronomy, University of Virginia, P.O. Box 400325, Charlottesville, VA 22904, USA
[14]National Radio Astronomy Observatory, 520 Edgemont Rd., Charlottesville VA 22903, USA
[15]Department of Physics and Astronomy, University of British Columbia
6224 Agricultural Road, Vancouver, BC V6T 1Z1, Canada

*This is the authors' version of the work. The definite version is published in *Science* Online, 26 April 2013, Vol: 340, Issue: 6131 doi: 10.1126/science.1233232

†Member of the International Max Planck Research School for Astronomy and Astrophysics at the Universities of Bonn and Cologne; e-mail: jantoniadis@mpifr-bonn.mpg.de

Many physically motivated extensions to general relativity (GR) predict significant deviations in the properties of spacetime surrounding massive neutron stars. We report the measurement of a 2.01±0.04 solar mass ($M_\odot$) pulsar in a 2.46-hr orbit with a 0.172±0.003 $M_\odot$ white dwarf. The high pulsar mass and the compact orbit make this system a sensitive laboratory of a previously untested strong-field gravity regime. Thus far, the observed orbital decay agrees with GR, supporting its validity even for the extreme conditions present in the system. The resulting constraints on deviations support the use of GR-based templates for ground-based gravitational wave detectors. Additionally, the system strengthens recent constraints on the properties of dense matter and provides insight to binary stellar astrophysics and pulsar recycling.

Neutron stars (NSs) with masses above $1.8\,M_\odot$ manifested as radio pulsars are valuable probes of fundamental physics in extreme conditions unique in the observable Universe and inaccessible to terrestrial experiments. Their high masses are directly linked to the equation-of-state (EOS) of matter at supra-nuclear densities (*1, 2*) and constrain the lower mass limit for production of astrophysical black holes (BHs). Furthermore, they possess extreme internal gravitational fields which result in gravitational binding energies substantially higher than those found in more common, $1.4\,M_\odot$ NSs. Modifications to GR, often motivated by the desire for a unified model of the four fundamental forces, can generally imprint measurable signatures in gravitational waves (GWs) radiated by systems containing such objects, even if deviations from GR vanish in the Solar System and in less massive NSs (*3–5*).

However, the most massive NSs known today reside in long-period binaries or other systems unsuitable for GW radiation tests. Identifying a massive NS in a compact, relativistic binary is thus of key importance for understanding gravity-matter coupling under extreme conditions. Furthermore, the existence of a massive NS in a relativistic orbit can also be used to test current knowledge of close binary evolution.

Results

PSR J0348+0432 & optical observations of its companion PSR J0348+0432, a pulsar spinning at 39 ms in a 2.46-hr orbit with a low-mass companion, was detected by a recent survey (*6, 7*) conducted with the Robert C. Byrd Green Bank Telescope (GBT). Initial timing observations of the binary yielded an accurate astrometric position, which allowed us to identify its optical counterpart in the Sloan Digital Sky Survey (SDSS) archive (*8*). The colors and flux of the counterpart are consistent with a low-mass white dwarf (WD) with a helium core at a distance of $d \sim 2.1$ kpc. Its relatively high apparent brightness ($g' = 20.71 \pm 0.03$ mag) allowed us to resolve its spectrum using the Apache Point Optical Telescope. These observations revealed deep Hydrogen lines, typical of low-mass WDs, confirming our preliminary identification. The radial velocities of the WD mirrored that of PSR J0348+0432, also verifying that the two stars are gravitationally bound.

In December 2011 we obtained phase-resolved spectra of the optical counterpart using the FORS2 spectrograph of the Very Large Telescope (VLT). For each spectrum, we measured the radial velocity which we then folded modulo the system's orbital period. Our orbital fit to the velocities constrains the semi-amplitude of their modulation to be $K_{\rm WD} = 351 \pm 4\,{\rm km\,s^{-1}}$ (Fig. 1; see also Materials & Methods). Similarly, the orbital solution from radio-pulsar timing yields $K_{\rm PSR} = 30.008235 \pm 0.000016\,{\rm km\,s^{-1}}$ for the pulsar. Combined, these constraints imply a mass ratio, $q = M_{\rm PSR}/M_{\rm WD} = K_{\rm WD}/K_{\rm PSR} = 11.70 \pm 0.13$.

Modeling of the Balmer-series lines in a high signal-to-noise average spectrum formed by the coherent addition of individual spectra (Fig. 1b) shows that the WD has an effective temperature of $T_{\rm eff} = (10120 \pm 47_{\rm stat} \pm 90_{\rm sys})\,{\rm K}$ and a surface gravity of $\log_{10}(g\,[{\rm cm\,s^{-2}}]) = (6.035 \pm 0.032_{\rm stat} \pm 0.060_{\rm sys})\,{\rm dex}$. Here the systematic error is an overall estimate of uncertainties due to our fitting technique and flux calibration (*8*). We found no correlation of this measurement with orbital phase and no signs of rotationally-induced broadening in the spectral lines (*8*). Furthermore, we searched for variability using the ULTRACAM instrument (*9*) on the 4.2-m William-Herschel Telescope at La Palma, Spain. The lightcurves, spanning 3 hours in total, have a root-mean-square scatter of ~ 0.53, 0.07 and 0.08 mag in u', g' and r' respectively and show no evidence for variability over the course of the observations. The phase-folded light-curve shows no variability either. Additionally, our calibrated magnitudes are consistent with the SDSS catalogue magnitudes, implying that the WD shone at a constant flux over this ~ 5 yr timescale (*8*).

Mass of the white dwarf The surface gravity of the WD scales with its mass and the inverse square of its radius ($g \equiv GM_{\rm WD}/R_{\rm WD}^2$). Thus, the observational constraints combined with a theoretical finite-temperature mass-radius relation for low-mass WDs yield a unique solution for the mass of the companion (*10*). Numerous such models exist in the literature, the most detailed of which are in good agreement for very low mass WDs ($< 0.17 - 0.18\,{\rm M_\odot}$), but differ substantially for higher masses [e.g. (*11–13*)]. The main reason for this is the difference in the predicted size of the hydrogen envelope, which determines whether the main energy source of the star is residual hydrogen burning (for "thick" envelopes) or the latent heat of the core (for "thin" envelopes).

In the most widely accepted scenario, WDs lose their thick hydrogen envelope only if their mass exceeds a threshold. The exact location of the latter is still uncertain but estimated to be around $\sim 0.17 - 0.22\,{\rm M_\odot}$ [e.g. (*11–13*)]. Two other pulsars with WD companions, studied in the literature, strongly suggest that this transition threshold is indeed most likely close to $0.2\,{\rm M_\odot}$ (*10, 14*). In particular, the WD companion of PSR J1909−3744 has a well-determined mass of $0.20\,{\rm M_\odot}$ (*15*), a large characteristic age of a several Gyr and a WD companion that appears to be hot (*10*), suggesting that its envelope is thick. For this reason we base the WD mass estimate on cooling tracks with thick hydrogen atmospheres for masses up to $0.2\,{\rm M_\odot}$, which we constructed using the "MESA" stellar evolution code (*8, 16*). Initial models were built for masses identical to the ones in (*11*) — for which previous comparisons have yielded good agreement with observations (*14*) — with the addition of tracks with 0.175 and $0.185\,{\rm M_\odot}$

for finer coverage (Fig. 2). For masses up to $0.169\,M_\odot$ our models show excellent agreement with (*11*); our $0.196\,M_\odot$ model though is quite different, because it has a thick envelope instead of a think one. Being closer to the constraints for the WD companion to PSR J0348+0432, it yields a more conservative mass constraint: $M_{\rm WD} = 0.165 - 0.185$ at 99.73% confidence (Fig. 3 & Table 1), which we adopt. The corresponding radius is $R_{\rm WD} = 0.046 - 0.092\,R_\odot$ at 99.73% confidence. Our models yield a cooling age of $\tau_{\rm cool} \sim 2\,$Gyr.

Pulsar mass The derived WD mass and the observed mass ratio q imply a NS mass in the range $1.97 - 2.05\,M_\odot$ at 68.27% or $1.90 - 2.18\,M_\odot$ at 99.73% confidence. Hence, PSR J0348+0432 is only the second NS with a precisely determined mass around $2\,M_\odot$, after PSR J1614−2230 (*2*). It has a 3-σ lower mass limit $0.05\,M_\odot$ higher than the latter, and therefore provides a verification, using a different method, of the constraints on the EOS of super-dense matter present in NS interiors (*2, 17*). For these masses and the known orbital period, GR predicts that the orbital period should decrease at the rate of $\dot{P}_{\rm b}^{\rm GR} = (-2.58^{+0.07}_{-0.11}) \times 10^{-13}\,{\rm s\,s^{-1}}$ (68.27% confidence) due to energy loss through GW emission.

Radio observations Since April 2011 we have been observing PSR J0348+0432 with the 1.4 GHz receiver of the 305-m radio telescope at the Arecibo Observatory, using its four Wideband Pulsar Processors (*18*). In order to verify the Arecibo data, we have been independently timing PSR J0348+0432 at 1.4 GHz using the 100-m radio telescope in Effelsberg, Germany. The two timing data sets produce consistent rotational models, providing added confidence in both. Combining the Arecibo and Effelsberg data with the initial GBT observations (*7*), we derive the timing solution presented in Table 1. To match the arrival times, the solution requires a significant measurement of orbital decay, $\dot{P}_{\rm b} = (-2.73 \pm 0.45) \times 10^{-13}\,{\rm s\,s^{-1}}$ (68.27% confidence).

The total proper motion and distance estimate (Table 1) allows us to calculate the kinematic corrections to $\dot{P}_{\rm b}$ from its motion in the Galaxy, plus any contribution due to possible variations of Newton's gravitational constant G: $\delta\dot{P}_{\rm b} = 0.016 \pm 0.003 \times 10^{-13}\,{\rm s\,s^{-1}}$. This is negligible compared to the measurement uncertainty. Similarly, the small rate of rotational energy loss of the pulsar (Table 1) excludes any substantial contamination due to mass loss from the system; furthermore we can exclude substantial contributions to $\dot{P}_{\rm b}$ from tidal effects (see (*8*) for details). Therefore, the observed $\dot{P}_{\rm b}$ is caused by GW emission and its magnitude is entirely consistent with the one predicted by GR: $\dot{P}_{\rm b}/\dot{P}_{\rm b}^{\rm GR} = 1.05 \pm 0.18$ (Fig. 3).

If we *assume* that GR is the correct theory of gravity, we can then derive the component masses from the intersection of the regions allowed by q and $\dot{P}_{\rm b}$ (Fig. 3): $M_{\rm WD} = 0.177^{+0.017}_{-0.018}\,M_\odot$ and $M_{\rm PSR} = 2.07^{+0.20}_{-0.21}\,M_\odot$ (68.27% confidence). These values are not too constraining yet. However, the uncertainty of the measurement of $\dot{P}_{\rm b}$ decreases with $T^{-5/2}$ (where T is the timing baseline); therefore this method will yield very precise mass measurements within a couple of years.

Discussion

PSR J0348+0432 as a testbed for gravity There are strong arguments for GR not to be valid beyond a (yet unknown) critical point, like its incompatibility with quantum theory and its prediction of the formation of spacetime singularities under generic conditions. Therefore, it remains an open question if GR is the final description of macroscopic gravity. This strongly motivates testing gravity regimes that have not been tested before, in particular regimes where gravity is strong and highly non-linear. Presently, binary pulsars provide the best high-precision experiments to probe strong-field deviations from GR and the best tests of the radiative properties of gravity (*19–23*). Among these systems PSR J0348+0432 has a special role: it is the first massive ($\sim 2\,M_\odot$) NS in a relativistic binary orbit. The orbital period of PSR J0348+0432 is only 15 seconds longer than that of the double pulsar system, but it has ~ 2 times more fractional gravitational binding energy than each of the double pulsar NSs. This places it far outside the presently tested binding energy range [see Fig. 4a & (*8*)]. Because the magnitude of strong-field effects generally depends non-linearly on the binding energy, the measurement of orbital decay transforms the system into a gravitational laboratory for a previously untested regime, qualitatively very different from what was accessible in the past.

In physically consistent and extensively studied alternatives, gravity is generally mediated by extra fields (e.g. scalar) in addition to the tensor field of GR (*5*). A dynamical coupling between matter and these extra fields can lead to prominent deviations from GR that only occur at the high gravitational binding energies of massive NSs. One of the prime examples is the strong-field scalarization discovered in (*3*). If GR is not valid, in the PSR J0348+0432 system where such an object is closely orbited by a weakly self-gravitating body, one generally expects a violation of the strong equivalence principle that in turn leads to a modification in the emission of gravitational waves. While in GR the lowest source multipole that generates gravitational radiation is the quadrupole, alternative gravity theories generally predict the presence of monopole and dipole radiation, on top of a modification of the other multipoles (*5*). For a binary system, the leading change in the orbital period is then given by the dipole contribution, which for a (nearly) circular orbit reads (*8*):

$$\dot{P}_{\rm b}^{\rm dipolar} \simeq -\frac{4\pi^2 G}{c^3 P_{\rm b}} \frac{M_{\rm PSR} M_{\rm WD}}{M_{\rm PSR} + M_{\rm WD}} \left(\alpha_{\rm PSR} - \alpha_{\rm WD}\right)^2 , \qquad (1)$$

where $\alpha_{\rm PSR}$ is the effective coupling strength between the NS and the ambient fields responsible for the dipole moment [e.g. scalar fields in scalar-tensor gravity], and $\alpha_{\rm WD}$ is the same parameter for the WD companion. The WD companion to PSR J0348+0432 has a fractional gravitational binding energy ($E_{\rm grav}/M_{\rm WD}c^2$) of just -1.2×10^{-5}, and is therefore a weakly self-gravitating object. Consequently, $\alpha_{\rm WD}$ is practically identical to the linear field-matter coupling α_0, which is well constrained ($|\alpha_0| < 0.004$) in Solar System experiments (*20, 24*).

For $\alpha_{\rm PSR}$, the situation is very different. Even if α_0 is vanishingly small, $\alpha_{\rm PSR}$ can have values close to unity, due to a non-linear behavior of gravity in the interaction between matter and the gravitational fields in the strong-gravity regime inside NSs (*3, 4*). A significant $\alpha_{\rm PSR}$

for NSs up to $1.47\,M_\odot$ has been excluded by various binary pulsar experiments (*8, 23*). The consistency of the observed GW damping ($\dot{P}_b$) with the GR predictions for PSR J0348+0432 (Table 1) implies $|\alpha_{PSR} - \alpha_0| < 0.005$ (95% confidence) and consequently excludes significant strong-field deviations, even for massive NSs of $\sim 2\,M_\odot$.

To demonstrate in some detail the implications of our results for possible strong-field deviations of gravity from Einstein's theory, we confront our limits on dipolar radiation with a specific class of scalar-tensor theories, in which gravity is mediated by a symmetric second-rank tensor field $g^*_{\mu\nu}$ and by a long-range (massless) scalar field φ. Scalar-tensor theories are well motivated and consistent theories of gravity, extensively studied in the literature [e.g. (*25, 26*)]. For this reason, they are the most natural framework for us to illustrate the gravitational phenomena that can be probed with PSR J0348+0432.

Concerning the EOS of NS matter, in our calculations we use the rather stiff EOS ".20"of (*27*) that supports (in GR) NSs of up to $2.6\,M_\odot$. We make this choice for two reasons: i) a stiffer EOS generally leads to more conservative limits when constraining alternative gravity theories, and ii) it is able to support even more massive NSs than PSR J0348+0432, which are likely to exist (*28–30*). Furthermore, in most of our conclusions a specific EOS is used only for illustrative purposes, and the obtained generic results are EOS independent.

Fig. 4b illustrates how PSR J0348+0432 probes a non-linear regime of gravity that has not been tested before. A change in EOS and gravity theory would lead to a modified functional shape for the effective coupling strength, α_{PSR}. However, this would not change the general picture: even in the strong gravitational field of a $2\,M_\odot$ NS gravity seems to be well described by GR and there is little space for any deviations, at least in the form of long-range fields, which influence the binary dynamics. Short range interactions, like massive Brans-Dicke gravity (*31*) with a sufficiently large scalar mass (heavier than $\sim 10^{-19}\,\mathrm{eV}/c^2$), cannot be excluded by PSR J0348+0432. Nevertheless, as we will argue below, in combination with the upcoming ground-based GW detectors, this could lead to particularly illuminating insights into the properties of gravitational interaction.

Constraints on the phase evolution of neutron-star mergers The first likely direct GW detection from astrophysical sources by ground-based laser interferometers, like the LIGO (Laser Interferometer Gravitational Wave Observatory, (*32*)) and the VIRGO (*33*) projects, will mark the beginning of a new era of GW astronomy (*34*). One of the most promising sources for these detectors are in-spiralling compact binaries, consisting of NSs and BHs, whose orbits are decaying towards a final coalescence due to GW damping. While the signal sweeps in frequency through the detectors' typical sensitive bandwidth between about 20 Hz and a few kHz, the GW signal will be deeply buried in the broadband noise of the detectors (*34*). To detect it, one will have to apply a matched filtering technique, i.e. correlate the output of the detector with a template wave form. Consequently, it is crucial to know the binary's orbital phase with high accuracy for searching and analyzing the signals from in-spiraling compact binaries. Typically, one aims to lose less than one GW cycle in a signal with $\sim 10^4$ cycles. For this reason, within GR such calculations have been conducted with great effort by various groups up to the 3.5 post-

Newtonian order, i.e. all (non-vanishing) terms up to order $(v/c)^7$, providing sufficient accuracy for a detection (*35–37*).

If the gravitational interaction between two compact masses is different from GR, the phase evolution over the last few thousand cycles, which fall into the bandwidth of the detectors, might be too different from the (GR) template in order to extract the signal from the noise. In scalar-tensor gravity for instance, the evolution of the phase is driven by radiation reaction, which is modified because the system loses energy to scalar GWs (*38, 39*). Depending on the difference between the effective scalar couplings of the two bodies, α_A and α_B, the 1.5 post-Newtonian dipolar contribution to the phase evolution could drive the GW signal many cycles away from the GR template. For this reason, it is desirable that potential deviations from GR in the interaction of two compact objects can be tested and constrained prior to the start of the advanced GW detectors. For "canonical" $1.4\,M_\odot$ NSs and long-range gravitational fields, this has already been achieved to a high degree in binary pulsar experiments, e.g. (*39*). So far, the best constraints on dipolar gravitational wave damping in compact binaries come from the observations of the millisecond pulsar PSR J1738+0333 (*23*). However, as discussed in detail above, these timing experiments are insensitive to strong-field deviations that might only become relevant in the strong gravitational fields associated with high-mass NSs. Consequently, the dynamics of a merger of a $2\,M_\odot$ NS with a "canonical" NS or a BH might have a significant contribution from dipolar GWs. With our constraints on dipolar radiation damping from the timing observations of PSR J0348+0432, given above, we can already exclude a deviation of more than ~ 0.5 cycles from the GR template during the observable in-spiral caused by additional long-range gravitational fields, for the whole range of NS masses observed in nature (see Fig. 5, and (*8*) for the details of the calculation). This compares to the precision of GR templates based on the 3.5 post-Newtonian approximation (*35, 37*). Furthermore, in an extension of the arguments in (*38, 39*) to massive NSs, our result implies that binary pulsar experiments are already more sensitive for testing such deviations than the upcoming advanced GW detectors.

Finally, as mentioned before, our results on PSR J0348+0432 cannot exclude dipolar radiation from short-range fields. Hence, if the range of the additional field in the gravitational interaction happens to lie between the wavelength of the GWs of PSR J0348+0432 and the wavelength of the merger signal ($\sim 10^9$ cm; $\sim 10^{-13}\,\mathrm{eV}/c^2$), then the considerations concerning the applicability of the GR template given here do not apply. On the other hand, in such a case the combination of binary pulsar and LIGO/VIRGO experiments can be used to constrain the mass of this extra field.

Formation, past and future evolution of the system The measured spin period P and spin-period derivative $\dot{P}$ of PSR J0348+0432, combined with the masses and orbital period of the system (Table 1), form a peculiar set of parameters that gives insight to binary stellar evolution. The short 2.46-hr orbital period is best understood from evolution via a common envelope where the NS is captured in the envelope of the WD progenitor, leading to efficient removal of orbital angular momentum on a short timescale of $\sim 10^3$ yr (*40*). This implies that the NS was born with an initial mass close to its current mass of $2.01\,M_\odot$, because very little accretion was

possible. Whereas the slow spin period of ~ 39 ms and the unusually strong magnetic field (*8*) of a few 10^9 G (Table 1) provide further support for this scenario, the low WD mass contradicts the standard common-envelope hypothesis by requiring a progenitor star mass smaller than $2.2\,M_\odot$, because more massive stars would leave behind more massive cores (*8, 41*). For such low donor star masses, however, the mass ratio of the binary components is close to unity, leading to dynamically stable mass transfer without forming a common envelope (*42, 43*). One potential solution to this mass discrepancy for common-envelope evolution is to assume that the original mass of the WD was $\geq 0.4\,M_\odot$ and that it was subsequently evaporated by the pulsar wind (*44*) when PSR J0348+0432 was young and energetic, right after its recycling phase (*8*). Such an evolution could also help explain the formation of another puzzling system, PSR J1744−3922 (*45*). However, we find that this scenario is quite unlikely given that the observed spectrum of the WD in PSR J0348+0432 only displays hydrogen lines, which is not expected if the WD was indeed a stripped remnant of a much more massive helium or carbon-oxygen WD. Furthermore, it is unclear why this evaporation process should have come to a complete stop when the WD reached its current mass of $0.17\,M_\odot$. A speculative hypothesis to circumvent the above-mentioned problems would be a common-envelope evolution with hypercritical accretion, where $\sim 0.6\,M_\odot$ of material was efficiently transferred to a $1.4\,M_\odot$ NS (*8, 46*).

An alternative, and more promising, formation scenario is evolution via a close-orbit low-mass X-ray binary (LMXB) with a $1.0 - 1.6\,M_\odot$ donor star that suffered from loss of orbital angular momentum due to magnetic braking (*43, 47, 48*). This requires a finely tuned truncation of the mass-transfer process which is not yet understood in detail, but is also required for other known recycled pulsars (*8*) with short orbital periods of $P_\mathrm{b} \leq 8$ hr and low-mass helium WD companions with $M_\mathrm{WD} \approx 0.14 - 0.18\,M_\odot$. The interplay between magnetic braking, angular momentum loss from stellar winds (possibly caused by irradiation) and mass ejected from the vicinity of the NS is poorly understood and current stellar evolution models have difficulties reproducing these binary pulsar systems. One issue is that the converging LMXBs most often do not detach but keep evolving with continuous mass transfer to more and more compact systems with $P_\mathrm{b} \leq 1$ hr and ultra-light donor masses smaller than $0.08\,M_\odot$.

Using the Langer stellar evolution code (*8*), we have attempted to model the formation of the PSR J0348+0432 system via LMXB evolution (Fig. 6). To achieve this, we forced the donor star to detach its Roche lobe at $P_\mathrm{b} \sim 5$ hr, such that the system subsequently shrinks in size to its present value of $P_\mathrm{b} \simeq 2.46$ hr due to GW radiation within 2 Gyr, the estimated cooling age of the WD. An illustration of the past and future evolution of PSR J0348+0432 from the two different formation channels is shown in Fig. 7.

An abnormality of PSR J0348+0432 in view of the LMXB model is its slow spin period of $P \sim 39$ ms and, in particular, the high value for the spin period derivative, $\dot{P} = 2.41 \times 10^{-19}\,\mathrm{s\,s^{-1}}$. These values correspond to an inferred surface magnetic flux density of $B \sim 2 \times 10^9$ G, which is high compared to most other recycled pulsars (*49*). However, a high B value naturally explains the slow spin period of PSR J0348+0432 from a combination of spin-down during the Roche-lobe decoupling phase (*50*) and subsequent magnetic dipole radiation from this high-magnetic-field pulsar (*8, 49*). Another intriguing question concerning this evolutionary channel is the

spread in NS masses. In the five currently known NS-WD systems with $P_b \leq 8\,\mathrm{hr}$, the NS masses span a large range of values, ranging from ~ 1.4 up to $2.0\,M_\odot$. The lower masses imply that the mass transfer during the LMXB phase is extremely inefficient — only about 30% of the material leaving the donor is accreted by the NS (*14, 15*). If this is indeed the case, and one assumes that the physical processes that lead to the formation of these systems are similar, it is likely that PSR J0348+0432 was born with an initial mass of $1.7 \pm 0.1\,M_\odot$, providing further support for a non-negligible fraction of NSs born massive (*41*).

Emission of GWs will continue to shrink the orbit of PSR J0348+0432 and in 400 Myr (when $P_b \simeq 23$ min) the WD will fill its Roche lobe and possibly leave behind a planet orbiting the pulsar (*51, 52*). Alternatively, if PSR J0348+0432 is near the upper-mass limit for NSs then a BH might form via accretion-induced collapse of the massive NS in a cataclysmic, γ-ray burst-like event (*53*).

Materials & Methods

Radial velocities and atmospheric parameters A detailed log of the VLT observations can be found in (*8*) (Figure S1 & Table S1). We extracted the spectra following closely the method used in (*14*) and compared them with template spectra to measure the radial velocities. Our best fits for the WD had reduced χ^2 minimum values of $\chi^2_{\mathrm{red,min}} = 1.0 - 1.5$ (*8*). Uncertainties were taken to be the difference in velocity over which χ^2 increases by $\chi^2_{\mathrm{red,min}}$ to account for the fact that $\chi^2_{\mathrm{red,min}}$ is not equal to unity (*14*). After transforming the measurements to the reference frame of the Solar System Barycenter (SSB), we folded them using the radio-timing ephemeris described below. We then fitted for the semi-amplitude of the radial velocity modulation, K_{WD}, and the systemic radial velocity with respect to the SSB, γ, assuming a circular orbit and keeping the time of passage through the ascending node, T_{asc}, fixed to the best-fit value of the radio-timing ephemeris. Our solution yields $K_{\mathrm{WD}} = 351 \pm 4\,\mathrm{km\,s^{-1}}$ and $\gamma = -1 \pm 20\,\mathrm{km\,s^{-1}}$ (*8*).

Details of the Balmer lines in the average spectrum of PSR J0348+0432, created by the coherent addition of the individual spectra shifted to zero velocity, are shown in Fig. 1b. We modeled the spectrum using a grid of detailed hydrogen atmospheres (*54*). These models incorporate the improved treatment of pressure broadening of the absorption lines presented in (*55*). As mentioned above, our fit yields $T_{\mathrm{eff}} = (10120 \pm 35_{\mathrm{stat}} \pm 90_{\mathrm{sys}})\,\mathrm{K}$ for the effective temperature and $\log_{10} g = (6.042 \pm 0.032_{\mathrm{stat}} \pm 0.060_{\mathrm{sys}})$ for the surface gravity (*8*). The χ^2 map shown in Fig. 2a is inflated to take into account systematic uncertainties. The average spectrum was also searched for rotational broadening. Using the analytic profile of (*56*) to convolve the model atmospheres, we scanned the grid of velocities $0 \leq v_r \sin i \leq 2000\,\mathrm{km\,s^{-1}}$ with a step size of $100\,\mathrm{km\,s^{-1}}$. The result is consistent with no rotation and our 1-σ upper limit is $v_r \sin i \leq 430\,\mathrm{km\,s^{-1}}$.

Modeling of the white-dwarf mass Low-mass WDs are thought to form naturally within the age of the Universe via mass transfer in a binary, either through Roche-lobe overflow or common-envelope evolution. In both cases, the WD forms when the envelope mass drops below a critical limit, which depends primarily on the mass of the stellar core, forcing the star to

contract and detach from its Roche lobe. After the contraction, the mass of the relic envelope is fixed for a given core mass, but further reduction of its size may occur shortly before the star enters the final cooling branch due to hydrogen shell flashes which force the star to re-expand to giant dimensions. Additional mass removal via Roche-lobe overflow as well as rapid shell hydrogen burning through the CNO cycle may then lead to a decrease of the envelope size and affect the cooling history and atmospheric parameters. To investigate the consequence of a reduced envelope size for the WD companion to PSR J0348+0432, we constructed WD models in which we treat the envelope mass as a free parameter (*8*). For the WD companion to PSR J0348+0432, an envelope mass below the critical limit for hydrogen fusion is not likely for two main reasons:

First, for a pure helium composition, the observed surface gravity translates to a WD mass of $\sim 0.15\,M_\odot$ and a cooling age of ~ 20 Myr, which is anomalously small. Such a small age would also imply a large increase in the birth and in-spiral rate of similar relativistic NS–WD systems (*57*). Furthermore, post-contraction flash episodes on the WD are not sufficient to remove the entire envelope. Therefore, creation of a pure helium WD requires large mass loss rates before the progenitor contracts, which is unlikely. For small progenitor masses ($\leq 1.5\,M_\odot$) large mass loss prevents contraction and the star evolves to a semi-degenerate companion on a nuclear timescale that exceeds the age of the Universe. For more massive progenitors ($> 1.5\,M_\odot$) the core grows beyond $\sim 0.17\,M_\odot$ in a short timescale and ultimately leaves a too-massive WD.

Second, even for envelope hydrogen fractions as low as $X_{\rm avg} = 10^{-6}$, the observed temperature and surface gravity cannot be explained simultaneously: The low surface gravity would again require a small mass of $\sim 0.15\,M_\odot$. However, in this case the surface hydrogen acts like an insulator, preventing the heat of the core from reaching the stellar surface. As a result, temperatures as high as 10000 K can only be reached for masses above $\sim 0.162\,M_\odot$.

Past a critical envelope mass, the pressure at the bottom of the envelope becomes high enough to initiate hydrogen-shell burning. The latter then becomes the dominant energy source and the evolutionary time-scale increases; the radius of the star grows by $\sim 50\%$ (depending on the mass), expanding further for larger envelopes. The dependence of the surface gravity on the radius implies that the observed value translates to a higher mass as the envelope mass increases. Therefore, the most conservative lower limit for the WD mass (and thus for PSR J0348+0432, given the fixed mass ratio) is obtained if one considers models with the absolute minimum envelope mass required for hydrogen burning. In this scenario, the mass of the WD is in the range $0.162 - 0.181\,M_\odot$ at 99.73% confidence (*8*). Despite this constraint being marginally consistent with our observations (*8*), it is not likely correct due to the high degree of fine-tuning.

For these reasons we have adopted the assumption that the WD companion to PSR J0348+0432 has a thick envelope as generally expected for WDs with such low surface gravity and high temperature.

Radio-timing analysis The Arecibo observing setup (*8*) and data reduction are similar to the well tested ones described in (*23*). Special care is taken with saving raw search data, which allows for iterative improvement of the ephemeris and eliminates orbital-phase dependent smear-

ing of the pulse profiles, which might contaminate the measurement of $\dot{P}_{\rm b}$ (*58*). From this analysis we derive 7773 independent measurements of pulse times of arrival (TOAs) with a root-mean-square (rms) uncertainty smaller than $10\,\mu$s. Similarly the Effelsberg observations yield a total of 179 TOAs with uncertainties smaller than $20\,\mu$s.

We use the TEMPO2 timing package (*59*) to derive the timing solution presented in Table 1, using 8121 available TOAs from GBT (*7*), Arecibo and Effelsberg. The motion of the radiotelescopes relative to the barycenter of the Solar System was computed using the DE/LE 421 Solar System ephemeris (*60*), published by the Jet Propulsion Laboratories. The orbit of PSR J0348+0432 has a very low eccentricity, therefore we use the "ELL1" orbital model (*61*) to describe the motion of the pulsar.

For the best fit, the reduced χ^2 of the timing residuals (TOA minus model prediction) is 1.66, a result similar to what is obtained in timing observations of other millisecond pulsars. The overall weighted residual rms is $4.6\,\mu$s. There are no unmodeled systematic trends in the residuals; either as a function of orbital phase or as a function of time. Therefore $\chi^2 > 1$ is most likely produced by under-estimated TOA uncertainties. We increased our estimated TOA uncertainties for each telescope and receiver to produce a reduced χ^2 of unity on short timescales; for our dominant dataset (Arecibo) the errors were multiplied by a factor of 1.3.

This produces more conservative estimates of the uncertainties of the timing parameters; these have been verified using the Monte Carlo statistical method described in (*23*): when all parameters are fitted, the Monte Carlo uncertainty ranges are very similar to those estimated by TEMPO2. As an example, TEMPO2 estimates $\dot{P}_{\rm b} = (-2.73 \pm 0.45) \times 10^{-13}$ s s^{-1} (68.27% confidence) and the Monte Carlo method yields $\dot{P}_{\rm b} = (-2.72 \pm 0.45) \times 10^{-13}$ s s^{-1} (68.27% confidence), in excellent agreement. The observed orbital decay appears to be stable; no higher derivatives of the orbital period are detected (*8*).

Table 1.

Observed and Derived Parameters for the PSR J0348+0432 system

Timing parameters for the PSR J0348+0432 system, indicated with their 1-σ uncertainties as derived by TEMPO2 where appropriate (numbers in parentheses refer to errors on the last digits). The timing parameters are calculated for the reference epoch MJD 56000, and are derived from TOAs in the range MJD 54872 – 56208.

*For these timing parameters we have adopted the optically derived parameters (see text for details).

Optical Parameters	
Effective temperature, $T_{\rm eff}$ (K)	$10120 \pm 47_{\rm stat} \pm 90_{\rm sys}$
Surface gravity, $\log_{10}(g[{\rm cm\,s^{-1}}])$	$6.035 \pm 0.032_{\rm stat} \pm 0.060_{\rm sys}$
Semi-amplitude of orbital radial velocity, $K_{\rm WD}$ (km s^{-1})	351 ± 4
Systemic radial velocity relative to the Sun, γ (km s^{-1})	-1 ± 20
Timing Parameters	
Right ascension, α (J2000)	$03^{\rm h}\ 48^{\rm m}\ 43^{\rm s}.639000(4)$
Declination, δ (J2000)	$+04^\circ\ 32'\ 11\farcs4580(2)$
Proper motion in right ascension, μ_α (mas yr^{-1})	+4.04(16)
Proper motion in declination, μ_δ (mas yr^{-1})	+3.5(6)
Parallax, π_d (mas)	0.47*
Spin frequency, ν (Hz)	25.5606361937675(4)
First derivative of ν, $\dot{\nu}$ (10^{-15} Hz s^{-1})	−0.15729(3)
Dispersion measure, DM (cm^{-3} pc)	40.46313(11)
First derivative of DM, DM1 (cm^{-3} pc yr^{-1})	−0.00069(14)
Orbital period, $P_{\rm b}$ (d)	0.102424062722(7)
Time of ascending node, $T_{\rm asc}$ (MJD)	56000.084771047(11)
Projected semi-major axis of the pulsar orbit, x (lt-s)	0.14097938(7)
$\eta \equiv e \sin\omega$	$(+1.9 \pm 1.0) \times 10^{-6}$
$\kappa \equiv e \cos\omega$	$(+1.4 \pm 1.0) \times 10^{-6}$
First derivative of $P_{\rm b}$, $\dot{P}_{\rm b}$ (10^{-12} s s^{-1})	−0.273(45)
Derived Parameters	
Galactic longitude, l	$183\fdg3368$
Galactic latitude, b	$-36\fdg7736$
Distance, d (kpc)	2.1(2)
Total proper motion, μ (mas yr^{-1})	5.3(4)
Spin period, P (ms)	39.1226569017806(5)
First derivative of P, $\dot{P}$ (10^{-18} s s^{-1})	0.24073(4)
Characteristic age, τ_c (Gyr)	2.6
Transverse magnetic field at the poles, B_0 (10^9 G)	~ 2
Rate or rotational energy loss, $\dot{E}$ (10^{32} erg s^{-1})	~ 1.6
Mass function, f ($M_\odot$)	0.000286778(4)
Mass ratio, $q \equiv M_{\rm PSR}/M_{\rm WD}$	11.70(13)
White dwarf mass, $M_{\rm WD}$ ($M_\odot$)	0.172(3)
Pulsar mass, $M_{\rm PSR}$ ($M_\odot$)	2.01(4)
"Range" parameter of Shapiro delay, r (μs)	0.84718*
"Shape" parameter of Shapiro delay, $s \equiv \sin i$	0.64546*
White dwarf radius, $R_{\rm WD}$ ($R_\odot$)	0.065(5)
Orbital separation, a (10^9 m)	0.832
Orbital separation, a ($R_\odot$)	1.20
Orbital inclination, i	$40\fdg2(6)$
$\dot{P}_{\rm b}$ predicted by GR, $\dot{P}_{\rm b}^{\rm GR}$ (10^{-12} s s^{-1})	$-0.258^{+0.008}_{-0.011}$
$\dot{P}_{\rm b}/\dot{P}_{\rm b}^{\rm GR}$	1.05 ± 0.18
Time until coalescence, τ_m (Myr)	~ 400

Figure 1.

Radial Velocities and Spectrum of the White Dwarf Companion to PSR J0348+0432. **Upper:** Radial velocities of the WD companion to PSR J0348+0432 plotted against the orbital phase (shown twice for clarity). Over-plotted is the best-fit orbit of the WD (blue line) and the mirror orbit of the pulsar (green). **Lower:** Details of the fit to the Balmer lines (Hβ to H12) in the average spectrum of the WD companion to PSR J0348+0432 created by the coherent addition of 26 individual spectra shifted to zero velocity. Lines from Hβ (bottom) to H12 are shown. The red solid lines are the best-fit atmospheric model (see text). Two models with $(T_{\rm eff}, \log_{10} g) = (9900\,{\rm K}, 5.70)$ and $(T_{\rm eff}, \log_{10} g) = (10200\,{\rm K}, 6.30)$, each $\sim$ 3-σ off from the best-fit central value (including systematics) are shown for comparison (dashed blue lines).

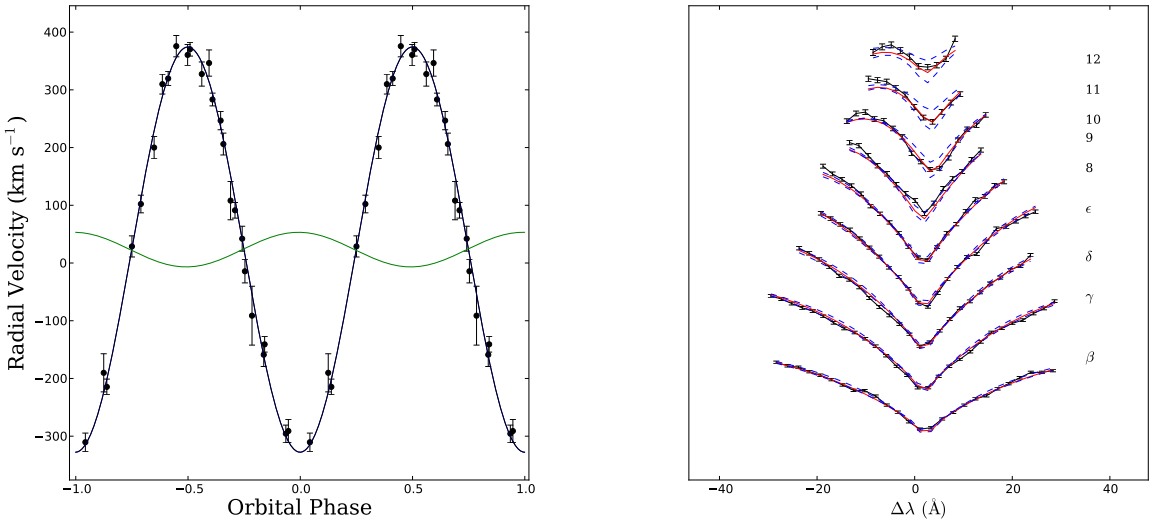

Figure 2.

Mass Measurement of the White Dwarf Companion to PSR J0348+0432

Left: Constraints on effective temperature, $T_{\rm eff}$, and surface gravity, g, for the WD companion to PSR J0348+0432 compared with theoretical WD models. The shaded areas depict the $\chi^2 - \chi^2_{\rm min} = 2.3$, 6.2 and 11.8 intervals (equivalent to 1, 2 and 3-σ) of our fit to the average spectrum. Dashed lines show the detailed theoretical cooling models of (*11*). Continuous lines depict tracks with thick envelopes for masses up to $\sim 0.2\,{\rm M}_\odot$ that yield the most conservative constraints for the mass of the WD. **Right:** Finite-temperature mass-radius relations for our models together with the constraints imposed from modeling of the spectrum (see text). Low mass – high temperature points are an extrapolation from lower temperatures.

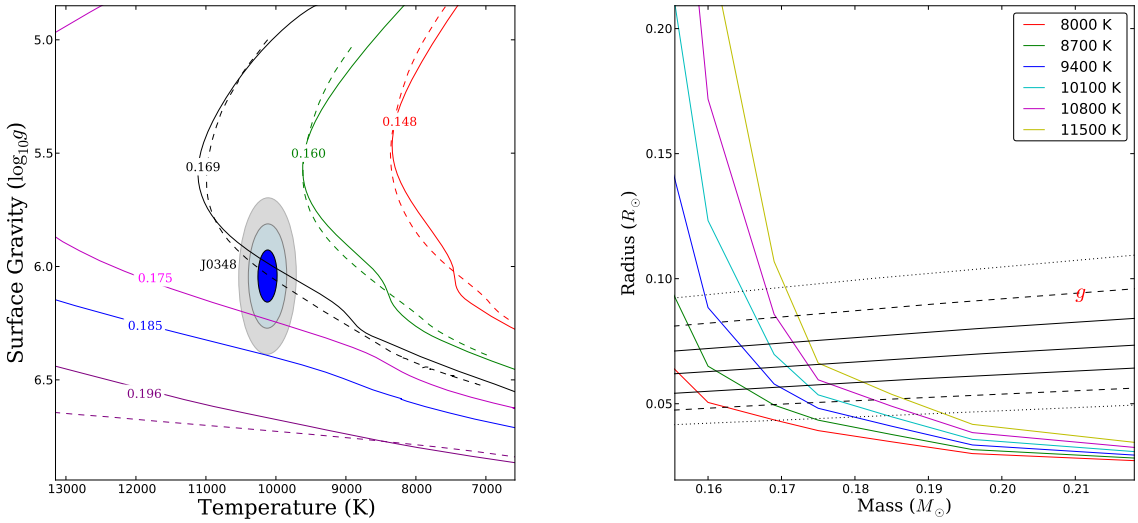

Figure 3.

System Masses and Orbital-Inclination Constraints

Constraints on system masses and orbital inclination from radio and optical measurements of PSR J0348+0432 and its WD companion. Each triplet of curves corresponds to the most likely value and standard deviations (68.27% confidence) of the respective parameters. Of these, two (the mass ratio q and the companion mass $M_{\rm WD}$) are independent of specific gravity theories (in black). The contours contain the 68.27 and 95.45% of the two-dimensional probability distribution. The constraints from the measured intrinsic orbital decay ($\dot{P}_{\rm b}^{\rm int}$, in orange) are calculated *assuming* that GR is the correct theory of gravity. All curves intersect in the same region, meaning that GR passes this radiative test (*8*). **Left**: $\cos i$–$M_{\rm WD}$ plane. The gray region is excluded by the condition $M_{\rm PSR} > 0$. **Right**: $M_{\rm PSR}$–$M_{\rm WD}$ plane. The gray region is excluded by the condition $\sin i \leq 1$. The lateral panels depict the one-dimensional probability-distribution function for the WD mass (right), pulsar mass (upper right) and inclination (upper left) based on the mass function, $M_{\rm WD}$ and q.

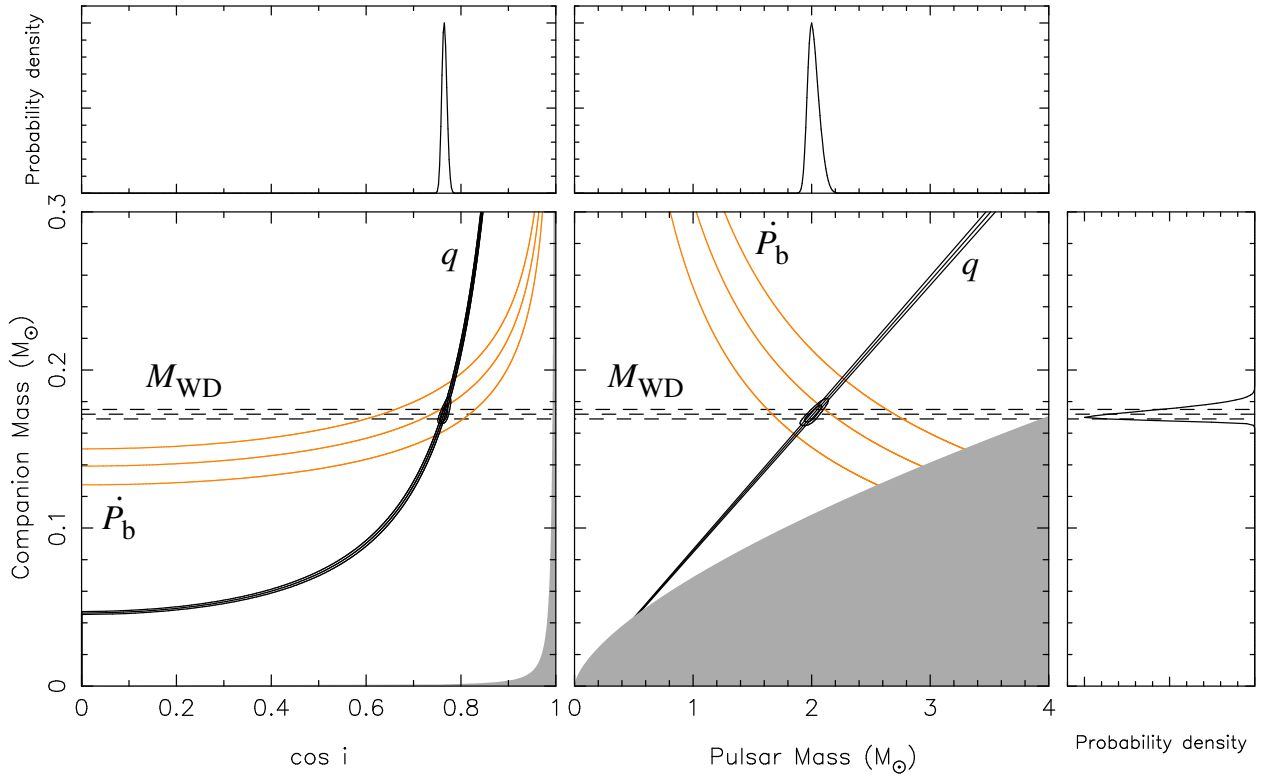

Figure 4.

Probing Strong Field Gravity with PSR J0348+0432

Left: Fractional gravitational binding energy as a function of the inertial mass of a NS in GR (blue curve). The dots indicate the NSs of relativistic NS-NS (in green) and NS-WD (in red) binary-pulsar systems currently used for precision gravity tests (*8*). **Right:** Effective scalar coupling as a function of the NS mass, in the "quadratic" scalar-tensor theory of (*4*). For the linear coupling of matter to the scalar field we have chosen $\alpha_0 = 10^{-4}$, a value well below the sensitivity of any near-future Solar System experiment [e.g. GAIA (*62*)]. The solid curves correspond to stable NS configurations for different values of the quadratic coupling β_0: -5 to -4 (top to bottom) in steps of 0.1. The yellow area indicates the parameter space allowed by the best current limit on $|\alpha_{\rm PSR} - \alpha_0|$ (*23*), while only the green area is in agreement with the limit presented here. PSR J0348+0432 probes deeper into the non-linear strong-field regime due to its high mass.

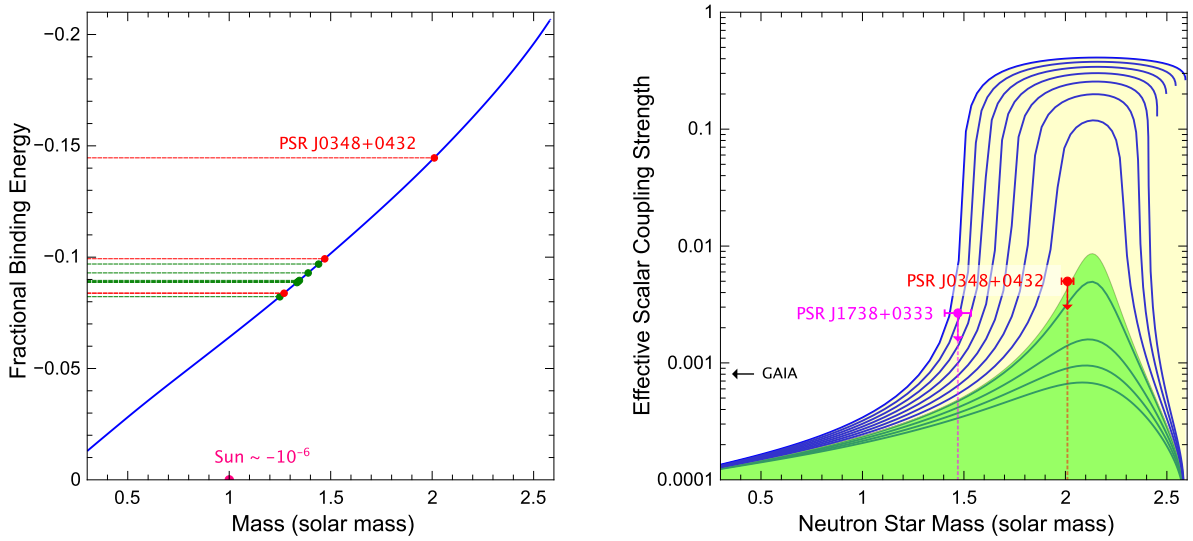

Figure 5.

Constraints on the Phase Offset in Gravitational Wave Cycles in the LIGO/VIRGO bands Maximum offset in GW cycles in the LIGO/VIRGO band (20 Hz to a few kHz) between the GR template and the true phase evolution of the in-spiral in the presence of dipolar radiation, as a function of the effective coupling of the massive NS for two different system configurations: a $2\,M_\odot$ NS with a $1.25\,M_\odot$ NS (NS-NS), and a merger of a $2\,M_\odot$ NS with a $10\,M_\odot$ BH (NS-BH). In the NS-NS case, the green line is for $\alpha_B = \alpha_0$, and the gray dotted line represents the most conservative, rather unphysical, assumption $\alpha_0 = 0.004$ and $\alpha_B = 0$ (*8*). In the NS-BH case, α_B is set to zero (from the assumption that the no-hair theorem holds). The blue line is for $\alpha_0 = 0.004$ (Solar System limit for scalar-tensor theories), and the purple line represents $\alpha_0 = 0$. The gray area to the right of the red line is excluded by PSR J0348+0432. In this plot there is no assumption concerning the EOS.

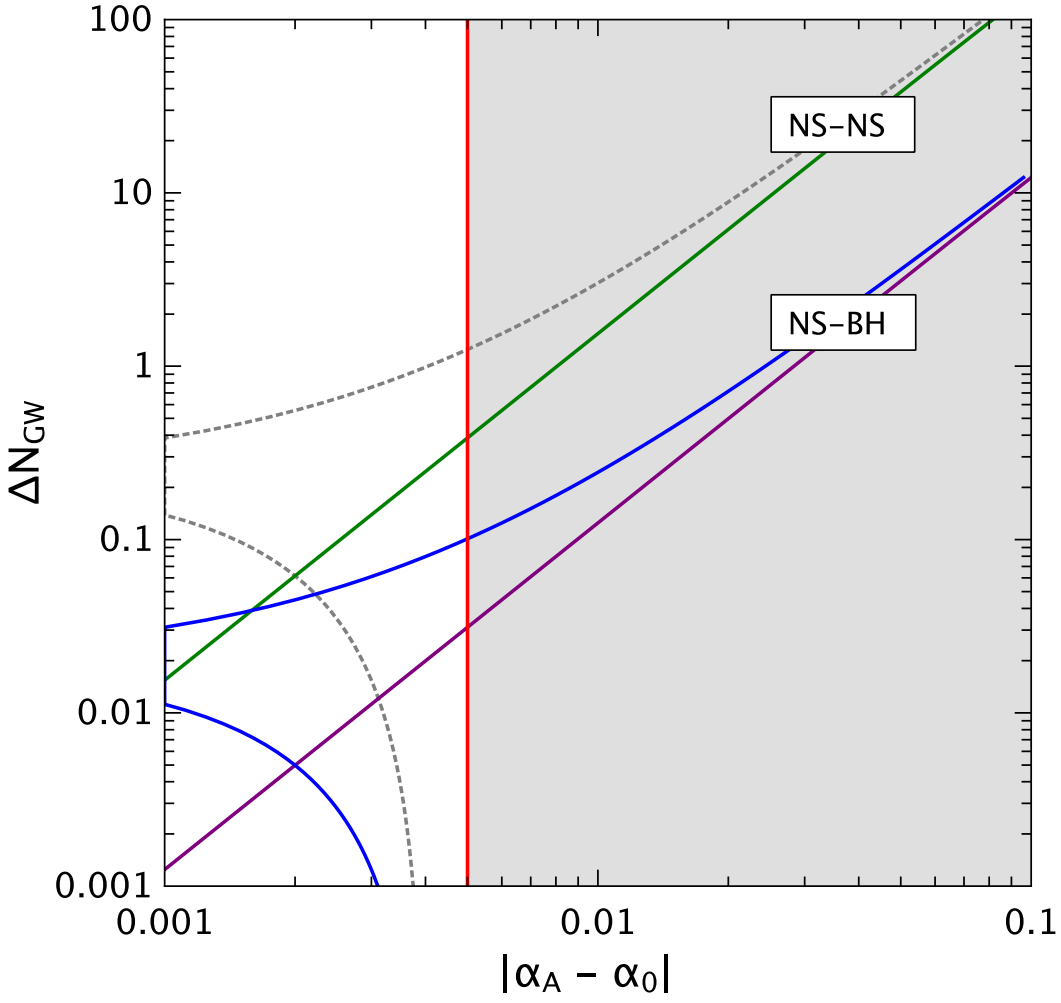

Figure 6.

Past and Future Orbital Evolution of PSR J0348+0432

Formation of PSR J0348+0432 from our converging LMXB model calculation. The plot shows orbital period as a function of time (calibrated to present day). The progenitor detached from its Roche lobe about 2 Gyr ago (according to the estimated cooling age of the WD) when $P_{\rm b} \simeq 5$ hr, and since then GW damping reduced the orbital period to its present value of 2.46 hr (marked with a star).

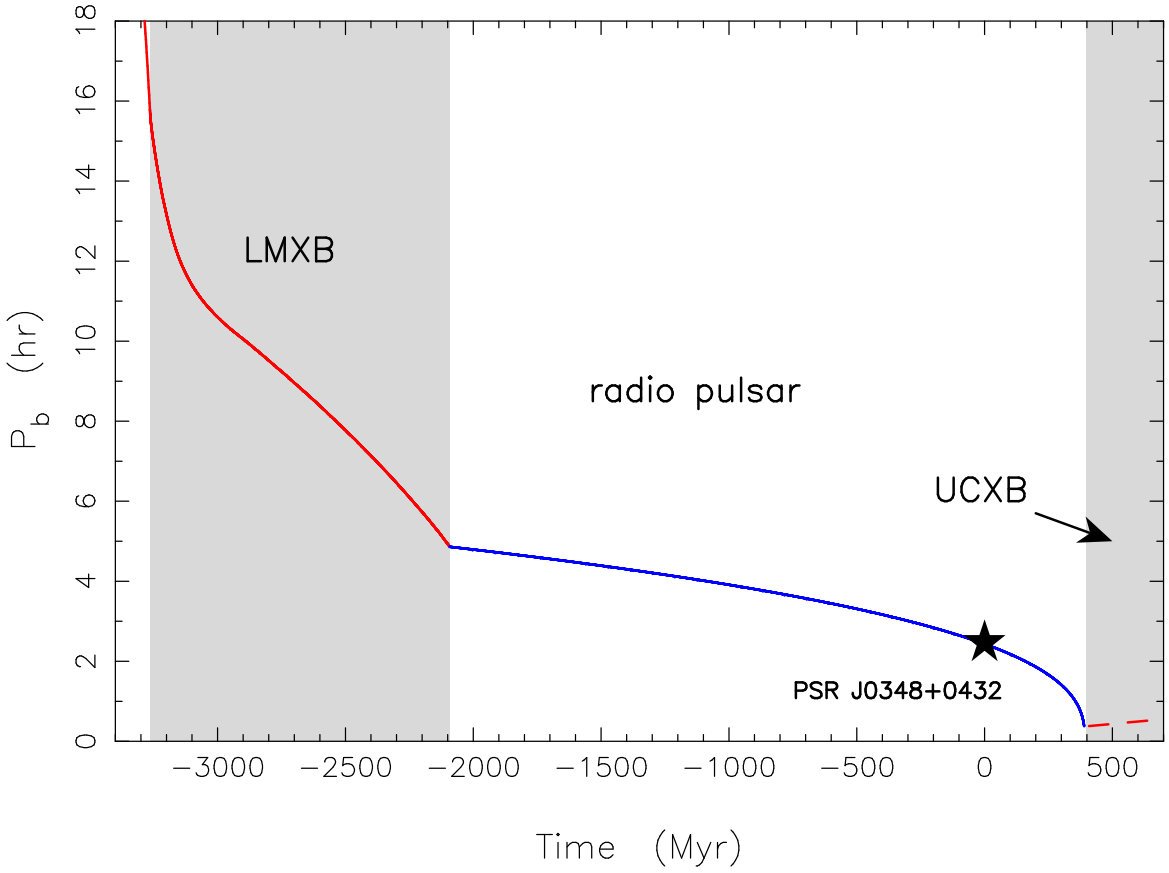

Figure 7.

Possible Formation Channels and Final Fate of PSR J0348+0432

An illustration of the formation and evolution of PSR J0348+0432. The zero-age main sequence (ZAMS) mass of the NS progenitor is likely to be 20 – 25 $M_\odot$, whereas the WD progenitor had a mass of 1.0 – 1.6 $M_\odot$ (LMXB) or 2.2 – 5 $M_\odot$ (common envelope, CE), depending on its formation channel. In ~ 400 Myr (when $P_b \simeq 23$ min) the WD will fill its Roche lobe and the system becomes an ultra-compact X-ray binary (UCXB) leading to the formation of a BH or a pulsar with a planet.

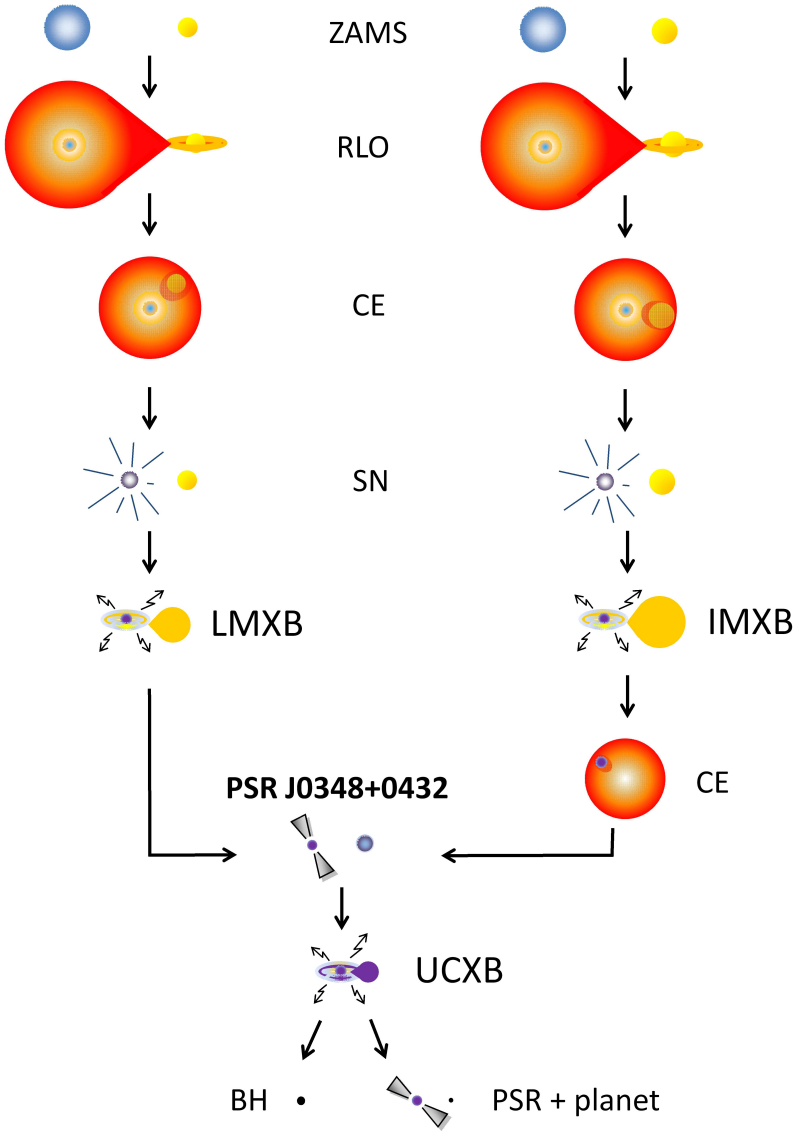

Supporting Online Material

VLT spectral observations and analysis We observed the companion of PSR J0348+0432 during December 19 & 20, 2011 with the FORS2 (*63*) instrument on Unite-Telescope 1 (Antú), using its blue sensitive E2V CCD detectors and the G1200B grism. This setup delivers a resolution of 0.36 Å per binned-by-two-pixel along dispersion and $0\farcs25$ per binned-by-two-pixel along the spatial direction. Because of the short orbital period of the binary, we chose a relatively wide $1''$ slit to avoid severe radial velocity smearing (by reducing the exposure time) and minimize possible dispersion losses not corrected by the dispersion corrector of the instrument. However, this choice may potentially result in systematic offsets in radial velocity measurements due to non-uniform illumination of the slit. To monitor these effects we rotated the slit by $134\fdg8$ (north-through east) with respect to the parallactic angle to include a bright nearby star for local flux and velocity calibration (Fig. S1). Our setup covers the spectral range from $\sim$ 3700 to 5200 Å with a resolution ranging from $\sim$ 2 to 3 Å depending on the seeing. During the first night the conditions were good to photometric and the seeing varied between $\sim 0\farcs7$ and $1\farcs2$. The second night was sporadically plagued with thin cirrus and the seeing ranged from $\sim 0\farcs9$ to $1\farcs7$. Bias, flat and Mercury-Cadmium (HgCd) frames for wavelength calibration were collected during day-time after each run. We collected a total of 34 spectra of the white dwarf companion to PSR J0348+0432 and the nearby comparison star. Of these, 22 had 800-s exposures and were taken with the slit rotated by the angle mentioned above, 4 were taken with 850-s exposures during bad weather instances and 8 with the slit rotated by a slightly different angle during experimental stages. In addition, we collected 2 spectra of the comparison through a wider, $2\farcs5$ slit and spectra of several flux standards at the beginning and the end of each run through both $1''$ and $2\farcs5$ slits.

We reduced the data using routines inside the Munich Image and Data Analysis System (MIDAS). Our analysis, from cosmetic corrections to extraction of spectra, is identical to that followed for the white dwarf companion to PSR J1738+0333 and is described in detail elsewhere (*14*). The dispersion solution has root-mean-square (rms) residuals of $\sim$ 0.03 Å for 18 lines. Flux calibration was performed separately for each night by comparing flux-standard observations (Table S1) with high S/N templates or appropriate white dwarf model spectra (*54*). Overall, the response curves from each standard are consistent with each other, with the largest differences (up to 10%) observed at short wavelengths ($\lambda \leq 4000$ Å); we use their average for flux calibration. Prior to the latter, we corrected the narrow-slit spectra for wavelength dependent slit losses using the wide slit spectra of the comparison and accounted for atmospheric extinction using the average extinction curve for La Silla.

Radial velocities We extracted the radial velocities of the white dwarf companion and the nearby comparison star following the procedure described in (*14*). First, we identified the nearby comparison star as being a type G1V star (with an uncertainty of about 2 subtypes) and used a high-resolution spectrum of the similar star HD 20807 (*64*) as a template. For the PSR J0348+0432 white-dwarf companion we fitted a high S/N spectrum with a grid of DA

model atmospheres (*54*), used the best-fit template to measure radial velocities, averaged the zero-velocity spectra and finally re-fitted the average spectrum to determine the final template. We scanned a grid of velocities from -800 to $+800\,\mathrm{km\,s^{-1}}$ with a step-size of $5\,\mathrm{km\,s^{-1}}$. The best fits had $\chi^2_{\mathrm{red,min}} = 1 - 1.5$ and $\chi^2_{\mathrm{red,min}} = 1.1 - 3.0$ for the comparison star. As described in the main paper, we scaled the errors to account for the fact that $\chi^2_{\mathrm{red,min}}$ was not equal to unity.

The velocities of the comparison star show a peak-to-peak variation of $\sim 40\,\mathrm{km\,s^{-1}}$, much higher than the typical $0.8\,\mathrm{km\,s^{-1}}$ measurement error. While we find no evidence for binarity, the measurements form 5 distinct groups, each of which display a variability only marginally higher than the formal errors. These coincide with blocks of observations interrupted for target repositioning. The scatter of velocities is therefore clearly related to the instrument and most probably associated with positioning uncertainties. For this reason we chose to use velocities relative to the comparison.

The best-fit solution using all available (barycentred) data gave $K_{\mathrm{WD}} = 346 \pm 6\,\mathrm{km\,s^{-1}}$ and a systemic velocity of $\delta\gamma = +8 \pm 4\,\mathrm{km\,s^{-1}}$ relative to the comparison with $\chi^2_{\mathrm{red,min}} = 2.78$ for 32 degrees of freedom (dof). However, 8 of the observations used here were taken with the slit at a different angle and the white dwarf's velocity relative to the comparison is thus most likely contaminated with an extra systematic shift due to slit rotation. For this reason we neglect these data. Using the homogeneous set of observations only and further rejecting one outlier with spuriously shaped continuum (no. 15 in Table S1) we obtain $K_{\mathrm{WD}} = 345 \pm 4\,\mathrm{km\,s^{-1}}$ and $\delta\gamma = +23 \pm 5\,\mathrm{km\,s^{-1}}$ respectively with $\chi^2_{\mathrm{red,min}} = 0.99$ for 23 degrees of freedom (Fig. 1a).

After correcting for the small effect of orbital smearing ($\sin(\pi\langle t_{\mathrm{exp}}\rangle/P_{\mathrm{b}})/(\pi\langle t_{\mathrm{exp}}\rangle/P_{\mathrm{b}}) = 0.98636$) we find a semi-amplitude of $K_{\mathrm{WD}} = 351 \pm 4\,\mathrm{km\,s^{-1}}$. The best-fit systemic velocity of PSR J0348+0432 using the raw white dwarf velocity measurements is $\gamma = -1 \pm 6\,\mathrm{km\,s^{-1}}$. Given the large scatter of the comparison's velocity we adopt $\gamma = -1 \pm 20\,\mathrm{km\,s^{-1}}$ with the uncertainty being a conservative estimate based on the scatter of the data.

Average spectrum and atmospheric parameters We scanned a grid of models covering effective temperatures from $T_{\mathrm{eff}} = 8000$ to $25000\,\mathrm{K}$ with a step-size of $250\,\mathrm{K}$ and surface gravities ranging from $\log g = 5.00$ to $\log g = 8.00$ with a step-size of $0.25\,\mathrm{dex}$. At each point of the grid we fitted for the normalization using a polynomial function of the wavelength to account for non-perfect flux calibration. Analysis of statistical errors is again identical to that followed for the white dwarf companion of PSR J1738+0333 (*14*). We achieved the best fit to higher Balmer lines when excluding the continuum regions between 4000 – 4050, 4180 – 4270 and 4400 – 4790 Å, which had small irregularities due to leftover detector imperfections: $T_{\mathrm{eff}} = 10120 \pm 35\,\mathrm{K}$ and $\log g = 6.042 \pm 0.032$ (1σ) with $\chi^2_{\mathrm{red,min}} = 1.02$. To estimate the influence of systematics we varied the degree of the polynomial used for normalization (1st to 5th degree), the spectral regions used for the fit (lines-only to whole spectrum) and the assumed spectral resolution (by steps of $\sim 5\%$). We also searched for velocity smearing by checking the consistency of the solution in an average of spectra taken close to orbital conjunction and an average of spectra taken close to the nodes. Finally, we fitted each line (from Hβ to H12) separately to verify the consistency of the fit over the spectrum and examined the influence

of our flux calibration by fitting the average uncalibrated spectrum. Overall, all tests gave fits consistent within statistical errors with only few exceptions that had (higher) central values that differed by 120 K and 0.11 dex compared to the numbers above. The good agreement is probably due to the high S/N of the spectrum. The values adopted in the main paper are based on the solution using a third degree polynomial and the systematic error is a conservative estimate based on the scatter of the different fits mentioned above.

Spectroscopic modeling and the "high $\log g$**" problem** Spectroscopic modeling of the Balmer lines in *higher* mass white dwarfs shows a spurious increase in surface gravity for stars with temperatures between $\sim$ 8000 and 11000 K. This well-known problem is linked to the incomplete treatment of convection in 1-D atmospheric models and disappears with the use of 3-D model atmospheres (*65, 66*). However, our modeling below shows that for the parameter space relevant to the PSR J0348+0432 companion, the atmosphere is not yet convective (e.g. convection sets in at $T_{\rm eff} \leq 9300$ K for $M_{\rm WD} = 0.17\,{\rm M}_{\odot}$). Therefore this problem is very unlikely to be relevant for the mass determination presented here.

Initial white-dwarf models To construct the white dwarf models presented in the main paper, we evolved solar composition stars (metal mass-fraction of $Z = 0.02$) with masses between 1.0 and 1.5 $\rm M_{\odot}$ and applied a large mass-loss wind at various points on the Red Giant Branch (RGB). To constrain the upper limit of the envelope mass expected from natural binary evolution, we removed the mass before the star enters the asymptotic RGB, letting the star evolve and contract naturally to become a white dwarf. Our upper limits agree well with the results of previous studies (*11, 12, 67*). Finally, to fully control the envelope mass of the white dwarf at the final stages of evolution we neglected hydrogen fusion through the CNO bi-cycle that is responsible for the hydrogen shell flashes[1].

In Fig. S2 we show the post-contraction white dwarf cooling age when $T_{\rm eff} = 10000$ K, as a function of the total hydrogen mass (after cessation of the mass transfer), for masses ranging from 0.155 to 0.185 $\rm M_{\odot}$. For low envelope masses, hydrogen burning cannot be initiated and the white dwarf quickly radiates the latent thermal energy of the core and cools in a few Myr. The thick-envelope modes presented in the main text were constructed as above.

Metallicity The metallicity of the white dwarf plays an important role in both regulating the CNO luminosity and changing the chemical profile of the stellar envelope. Qualitatively, our main models described above are in good agreement with the $Z = 0.001$ models of (*69*) for the parameter space relevant to the white dwarf companion to PSR J0348+0432. Specifically, their 0.172 $\rm M_{\odot}$ track has a thick envelope and predicts a surface gravity of $\log g = 6.13$ for $T_{\rm eff} = 10000$ K which is reached at a cooling age of $\tau_{\rm cool} = 2.85$ Gyr. This agreement is not surprising given that CNO burning is neglected in our analysis, convective mixing has not yet set

[1]For a white dwarf at the final cooling branch, CNO luminosity accounts for less than 5% of the total energy budget. Hence, it is safe to neglect it without influencing the macroscopic characteristics of the models (*68*).

in at $T = 10000\,\mathrm{K}$ and consequently metals are absent from surface layers due to gravitational settling. Therefore we consider that any uncertainties due to metallicity are small and anyway included in our adopted errors.

Input physics of the stellar evolution models Stellar models used in our analysis were constructed using the 1-D stellar evolution code "`star`" provided with the Modules for Experiments in Stellar Astrophysics (MESA) (*16*). `star` solves for the equations of hydrostatic equilibrium, nuclear energy generation, convection and time-dependent element diffusion using a self-adaptive non-Lagrangian mesh and analytic Jacobians. We used default options for the equation-of-state, radiative and neutrino opacities, thermonuclear and weak reaction rates described in (*16*) and references therein. We implemented the mixing length theory of convection from (*70*) that takes into account radiative losses near the outer layers of the star. Diffusion was taken into account using the method and coefficients from (*71*) and transport of material was calculated using the method described in (*72*) after grouping the elements in "classes" in terms of atomic mass ranges. Finally, boundary atmospheric conditions were calculated using the gray-atmosphere approach of (*73*).

Photometry A photometric campaign on the white dwarf companion to PSR J0348+0432 was carried out during February 1, 2012 using the ULTRACAM instrument (*9*) on the 4.2-m William-Herschel Telescope at La Palma, Spain. The data were reduced using the standard ULTRACAM pipeline (Fig. S3).

The lightcurves have an rms scatter of ∼0.53, 0.07 and 0.08 mag in u', g' and r' respectively and show no evidence for variability over the course of the observations. The phase-folded light-curve shows no variability either. Additionally, our calibrated magnitudes are consistent with the SDSS catalogue magnitudes implying no significant variability at the ~ 5 yr time-scale.

Qualitatively, this result supports the use of the PSR J0348+0432 system as a gravitational laboratory (see timing analysis below). In what follows, we discuss the limits on various parameters in more detail. Three effects that cause phase-dependent variability are: deformation of the white dwarf by tides raised by the neutron star, irradiation by the pulsar wind, and Doppler boosting caused by the white dwarf's orbital motion. For a circular orbit, the combined modulation in photon rate n_γ is given by

$$\Delta n_\gamma / n_{\gamma,0} \simeq f_{\rm ell}\left(\frac{R_{\rm WD}}{a}\right)^3 q \sin^2 i \cos(4\pi\phi) + f_{\rm db}\frac{K_{\rm WD}}{c}\sin i\cos(2\pi\phi) - f_{\rm irr}\frac{T_{\rm irr}^4}{32T_{\rm eff}^4}\sin i \sin(2\pi\phi), \quad (2)$$

with $f_{\rm ell}$, $f_{\rm db}$, and $f_{\rm irr}$ factors of order unity describing the observability in a given filter, $0 \le \phi \le 1$ the orbital phase, and $T_{\rm irr} = L_{\rm psr}/4\pi a^2\sigma \simeq 2400\,\mathrm{K}$ the effective temperature corresponding to the pulsar flux incident on the white dwarf. We find that all terms should be small. For the tidal deformation, $f_{\rm ell} = -3(15+u_1)(1+\tau_1)/20(3-u_1) = 1.75$, where we use linear approximations for limb and gravity darkening, with coefficients $u_1 = 0.36$ (*74*) and $\tau_1 = 1$ (appropriate for a radiative atmosphere). Thus, the expected modulation is 1.5×10^{-3}. For the Doppler boosting,

approximating the white dwarf as a black-body emitter, $f_{\rm db} \simeq \alpha \exp\alpha/(\exp\alpha - 1) \simeq 2.6$, where $\alpha = hc/\lambda kT_{\rm eff} \simeq 2.8$ (*75*), with $\lambda \simeq 550\,$nm the typical observing wavelength. Hence, the expected amplitude is $\sim 3 \times 10^{-3}$. Finally, for the irradiation, $f_{\rm irr} = (1 - A) f_{\rm db} \leq 2$, where the maximum is for albedo $A \simeq 0$. Thus, irradiation could cause a modulation of up to $\sim 1.2 \times 10^{-4}$.

Fitting the observed lightcurves with a function of the form $\Delta n_\gamma/\langle n_\gamma \rangle = 1 + a_{\rm ell}\cos(4\pi\phi) + a_{\rm db}\cos(2\pi\phi) - a_{irr}\sin(2\pi\phi)$, we find good fits ($\chi^2_{\rm red} \simeq 1$) but no significant detections, with averaged amplitudes of the higher S/N r and g band lightcurves of $a_{\rm ell} = 0.003 \pm 0.003$, $a_{\rm db} = 0.003 \pm 0.003$ and $a_{\rm irr} = 0.006 \pm 0.004$. The marginal irradiation signal would correspond to a temperature difference between the irradiated and non-irradiated side of $\sim 100\,$K, which is substantially larger than the expected difference of 2 K. Even if confirmed, however, this would not affect our inferred radial velocity amplitude or white dwarf parameters.

Finally, another possible source of variability is quadrupole moment variations of the white dwarf (*68*): these typically change the star's luminosity by a few per-cent (e.g. $\sim 20\%$ for the only three known cases of pulsating low-mass white dwarfs (*76, 77*)) and result in changes of the orbital period $P_{\rm b}$ through classical spin-orbit coupling (*78*). To our knowledge, all possible mechanisms for such variations would result in modulations much higher than the precision of our lightcurve. Therefore we can neglect this effect and assume that the star is in equilibrium. Our assumption is further supported by the lack of second or higher-order derivatives in the measured orbital period (see below) and recent theoretical findings (*79*) that locate the instability strip for g-mode oscillations outside the parameter space relevant for the white dwarf companion to PSR J0348+0432.

The SDSS photometry places a constraint on the distance to the system. Adopting the model of (*80*) for the interstellar reddening and the $0.169\,M_\odot$ cooling track of (*11*), we find that the luminosities (Fig. S3) are consistent with a distance of $d \simeq 2.1\,$kpc (and a reddening of $A_{\rm V} \sim 0.7$). Given the uncertainties in the models the error is difficult to estimate but it should be better than $\sim 10\%$. Our estimate is also consistent with the distance of $d_{\rm DM} \sim 2\,$kpc implied by the dispersion measure (DM) of the pulsar and the NE2001 model for the Galactic free electron density (*81*).

Radio observations The observing setup for the Arecibo telescope is identical to the well-tested setup described in (*23*), with the exception of one WAPP now being centered at 1610 MHz instead of 1310 MHz; the former band is cleaner and its use improves the precision of our DM measurements. Also, as in the former case, data are taken in search mode and processed off-line. This allows for iterative improvement of the pulsar ephemeris which is important at the early stages when the timing parameters are not yet very precise. With each improved ephemeris, we de-disperse and re-fold the data, obtaining pulse profiles with higher S/N that yield more accurate pulse times-of-arrival (TOAs). This helps to avoid orbital-phase dependent smearing and timing artefacts, which may corrupt the determination of orbital parameters, particularly the orbital phase and orbital period variation (*58*).

We de-disperse and fold the radio spectra following the procedure described in (*23*). TOAs are derived every 4 minutes to preserve the orbital information in the signal. The pulse profile

template, resulting from more than 1 hour of data, is displayed in Fig. 4. Although the pulse profile changes significantly from 350 to 2200 MHz (*7*), the changes within the band of the L-wide receiver used for timing (1100-1660 MHz, also displayed in Fig. 4) are small enough for us to consider this single average profile taken at 1410 MHz as a good template for all the data. The latter is cross-correlated with every 4-minute/25 MHz-wide pulse profile in the Fourier domain (*82, 83*) and the phase offset that yields the best match is used to derive the topocentric TOA of a reference sub-pulse (normally that closest to the start of each sub-integration). The results described below are obtained using 7773 TOAs with stated rms uncertainty smaller than $10\,\mu$s.

In order to verify the Arecibo data we have been timing PSR J0348+0432 with the 100-m radio telescope in Effelsberg, Germany, which has a very different observing system. The polarization characterization of the radio emission of PSR J0348+0432, displayed in the top plot of Fig. 4, was made with this telescope. Overlaid on the polarization data is a theoretical Rotating Vector Model (RVM). It is generally difficult to fit a RVM model to polarization data from recycled pulsars, but for PSR J0348+0432 this model works surprisingly well. For instance, as explained in (*82*), the covariance between the angle between the spin and magnetic axis, α, and the angle between the spin axis and the line of sight ζ, allows for a wide range of possible solutions (Fig. S5). However, if we assume that during the accretion episode that recycled the pulsar the spin axis of the pulsar was aligned with the orbital angular momentum (which has an angle $i = 40\overset{\circ}{.}2 \pm 0\overset{\circ}{.}6$ to the line of sight) then $\alpha \simeq 45^\circ$. The minimum angle between the magnetic axis and the line of sight is then given by $\beta = \zeta - \alpha = -5\overset{\circ}{.}$.

Apart from the polarimetry, the Effelsberg data yielded a total of 179 high-quality TOAs. As can be seen in Fig. 6, these follow the Arecibo timing very closely, providing added confidence in both.

Timing analysis The combined timing dataset contains 8121 TOAs. The TOA residuals obtained with the best ephemeris (Table 1) are displayed as a function of time in the top panel and as a function of orbital phase in the bottom plot of Fig. 6. To derive the ephemeris in Table 1 (using TEMPO2) we increased the TOA uncertainties by factors of 1.3 for the GBT and Arecibo data and by 1.8 for the Effelsberg data. This results in the residuals of each dataset having a normalized χ^2 of 1. Using these slightly increased (but more realistic) TOA uncertainties results in more conservative (i.e. larger) uncertainties for the fitted timing parameters. Globally, the residuals have a weighted rms of $4.6\,\mu$s and the reduced χ^2 is 1.019 for 8102 degrees of freedom. The TOA uncertainties presented in Fig. 6 are those used to derive the timing solution.

The orbit of PSR J0348+0432 has a very low eccentricity, therefore we use the "ELL1" orbital model (*61*) to parametrize it.[2] This parametrization yields Keplerian and post-Keplerian parameters very weakly correlated with each other. In order to estimate the intrinsic ("real")

[2]The ELL1 timing model as implemented in the TEMPO2 software package is a modification of the DD timing model (*84, 85*) adapted to low-eccentricity binary pulsars. In terms of post-Keplerian observables, it contains all those which are numerically relevant for systems with $e \ll 1$. The "Einstein delay" term is not relevant for such systems and is therefore not taken into account.

eccentricity of the binary (Table 1) we adopt $M_{\rm WD} = 0.172\,{\rm M}_\odot$ and $i = 40\overset{\circ}{.}2$ obtained from the optical observations. This assumption is safe because GR is known to provide a sufficiently accurate description of spacetime around weakly self-gravitating objects (*86*). According to (*87*), the orthometric amplitude of the Shapiro delay (which quantifies the time amplitude of the *measurable* part of the Shapiro delay) is $h_3 = 42\,{\rm ns}$. Fitting for this quantity we obtain $h_3 = 69 \pm 53\,{\rm ns}$. This is 1-$\sigma$ consistent with the prediction but the low relative precision of this measurement implies that we cannot determine $M_{\rm WD}$ and $\sin i$ independently from the existing timing data. A precise measurement of the component masses of this system from Shapiro delay would require an improvement in timing precision that is much beyond our current capabilities.

Intrinsic orbital decay As described in the main text, we detect an orbital decay consistent with the prediction of General Relativity. When we say that this decay is stable, we mean that we detect no higher-order variations of the orbital frequency $f_{\rm b} \equiv 1/P_{\rm b}$ nor large variations in $x \equiv a_p \sin i/c$:

$$\frac{d^2 f_{\rm b}}{dt^2} = -4.5 \pm 4.4 \times 10^{-23}\,{\rm Hz\,s^{-2}}, \quad (3)$$

$$\frac{d^3 f_{\rm b}}{dt^3} = +4.1 \pm 2.5 \times 10^{-36}\,{\rm Hz\,s^{-3}}, \quad (4)$$

$$\frac{dx}{dt} = +7.4 \pm 4.4 \times 10^{-15}\,{\rm s\,s^{-1}}, \quad (5)$$

where the values and 1-σ uncertainties were obtained using the TEMPO implementation of the BTX orbital model. In systems where the quadrupole moment of the white dwarf changes, we should expect such timing effects (*88*) plus significant photometric variations with orbital phase (discussed above). Since none are observed, the companion to PSR J0348+0432 is very likely to have a stable quadrupole moment.

The constraints on the total proper motion μ combined with the optically derived distance $d = 2.1 \pm 0.2\,{\rm kpc}$ allow us to calculate the two kinematic corrections to the observed $\dot{P}_{\rm b}$. The more important one is the Shklovskii effect (*89*):

$$\dot{P}_{\rm b}^{\rm Shk} = P_{\rm b}\frac{\mu^2 d}{c} = 0.0129^{+0.0025}_{-0.0021} \times 10^{-13}\,{\rm s\,s^{-1}}, \quad (6)$$

where we have adopted the 10% error-estimate on the distance. The second correction is caused by the difference of Galactic accelerations between the binary and the Solar System. Using the detailed procedure outlined in (*23*), we obtain:

$$\dot{P}_{\rm b}^{\rm Acc} = P_{\rm b}\frac{a_c}{c} = 0.0037^{+0.0006}_{-0.0005} \times 10^{-13}\,{\rm s\,s^{-1}}. \quad (7)$$

A third correction could arise from a possible variation of the gravitational constant $\dot{G}$. Conservative limits are given by (*90–93*):

$$\dot{P}_{\rm b}^{\dot{G}} = -2P_{\rm b}\frac{\dot{G}}{G} = (0.0003 \pm 0.0018) \times 10^{-13}\,{\rm s\,s^{-1}}, \quad (8)$$

where we used the latest limit on $\dot{G}$ from Lunar Laser Ranging (*94*).

Adding these corrections, we obtain a total of $\sim (+1.6 \pm 0.3) \times 10^{-15}\,\mathrm{s\,s^{-1}}$, or about 0.006 of the measured value. This is much smaller than the current measurement uncertainty and therefore we can conclude that, at the current precision limit, the observed value is intrinsic to the system. Its magnitude is entirely consistent with the GR prediction for the orbital decay caused by emission of gravitational waves: $\dot{P}_\mathrm{b}/\dot{P}_\mathrm{b}^\mathrm{GR} = 1.05 \pm 0.18$. This agreement is depicted graphically in a $\cos i - M_\mathrm{WD}$ and $M_\mathrm{PSR} - M_\mathrm{WD}$ diagram (Fig. 3); the consequences are discussed in the main paper and in detail further below.

Mass loss contribution to $\dot{P}_\mathrm{b}$ If the system is losing mass, that should cause a change in the orbital period (*91*):

$$\dot{P}_b^{\dot{M}} = 2\frac{\dot{M}_\mathrm{T}}{M_\mathrm{T}} P_\mathrm{b}, \tag{9}$$

where $\dot{M}_\mathrm{T} = \dot{M}_\mathrm{PSR} + \dot{M}_\mathrm{WD}$ is the change of mass of both components.

We now estimate both mass loss terms. The pulsar is losing rotational energy at a rate given by $\dot{E} = 4\pi I_\mathrm{PSR} \dot{P} P^{-3} = 1.6 \times 10^{32}\,\mathrm{erg\,s^{-1}}$, where I_PSR is the pulsar's moment of inertia, normally assumed to be $10^{45}\,\mathrm{g\,cm^2}$. This dominates the mass loss for the pulsar (*91*):

$$\frac{\dot{M}_\mathrm{PSR}}{M_\mathrm{T}} = \frac{\dot{E}}{M_\mathrm{T} c^2} = 4.1 \times 10^{-23}\,\mathrm{s^{-1}}. \tag{10}$$

Most of this energy is emitted as a wind of relativistic particles, which we assume to be isotropic to first order. A fraction of this energy $F = R_\mathrm{WD}^2/4a^2 = 0.00074$ (where $a = xc(q+1)/\sin i = 8.32 \times 10^8\,\mathrm{m}$ is the separation between components) strikes the surface of the white dwarf. This is the energy available to power mass loss from the white dwarf. Conservation of energy requires that

$$\dot{E} F = \frac{1}{2} \dot{M}_\mathrm{WD} v^2, \tag{11}$$

where v is the velocity of the escaping particles. This equation shows that $\dot{M}$ increases as v decreases, however v must be at least equal to the escape velocity for the star to lose mass, i.e., $v^2/2 > GM_\mathrm{WD}/R_\mathrm{WD}$. Putting all the constraints together, we obtain:

$$\frac{\dot{M}_\mathrm{WD}}{M_\mathrm{T}} < 5.4 \times 10^{-21}\,\mathrm{s^{-1}}. \tag{12}$$

Therefore, $\dot{M}_\mathrm{T} \simeq \dot{M}_\mathrm{WD}$. Evaluating eq. 9, we obtain $\dot{P}_b^{\dot{M}} < 0.4 \times 10^{-16}$, which is $\sim 5 \times 10^2$ times smaller than the current uncertainty in the measurement of $\dot{P}_\mathrm{b}$.

Tidal contribution to $\dot{P}_\mathrm{b}$ We now calculate the orbital decay caused by tides. If these change the angular velocity of the white dwarf $\dot{\Omega}_\mathrm{WD}$, this will be compensated by a change in the orbital

period of the system $\dot{P}_{\rm b}^{\rm T}$. We can relate the two because of conservation of angular momentum:

$$\dot{P}_{\rm b}^{\rm T} = \frac{3k\Omega_{\rm WD}}{2\pi q(q+1)}\left(\frac{R_{\rm WD}P_{\rm b}\sin i}{xc}\right)^2\frac{1}{\tau_s}, \tag{13}$$

where $\tau_s = -\Omega_{\rm WD}/\dot{\Omega}_{\rm WD}$ is the synchronization timescale and $k \equiv I_{\rm WD}/(M_{\rm WD}R_{\rm WD}^2)$, where $I_{\rm WD}$ is the white dwarf moment of inertia. For idealized white dwarfs (particularly those with a mass much below the Chandrasekhar limit) sustained solely by degeneracy pressure of non-relativistic electrons, a polytropic sphere with $n = 1.5$ provides a good approximation. For such stars, we have $k = 0.2$ (*95*). However, for this light white dwarf only the core is degenerate, and is surrounded by a deep non-degenerate layer that accounts for only about 5% of the mass of the star. Therefore, the mass distribution is much more centrally condensed than for an $n = 1.5$ polytrope and the moment of inertia is much smaller. We therefore use the output of our white dwarf model calculations (see Fig 2. and above) to estimate that factor. For the model closer to the mean of the white dwarf mass distribution, with $M_{\rm WD} = 0.169\,{\rm M}_\odot$, $R_{\rm WD} = 0.069\,{\rm R}_\odot$ and $T_{\rm eff} = 9950\,{\rm K}$ we obtain $k = 0.0267$. We adopt this value in subsequent calculations.

The only unknown parameters in this expression are $\Omega_{\rm WD}$ and τ_s. If τ_s were much smaller than the characteristic age of the pulsar $\tau_c = 2.6\,{\rm Gyr}$ (which is similar to the cooling age of the white dwarf, i.e., this number is likely to be a good approximation to the true age of the system), then the white dwarf rotation would already be synchronized with the orbit ($\Omega_{\rm WD} = 2\pi/P_{\rm b}$). In this case the orbital decay would be slightly affected because, as the orbital period decreases, the white dwarf spin period would decrease at exactly the same rate in order to preserve tidal locking. The resulting exchange of angular momentum would change the orbital decay by a factor $\Delta\dot{P}_{\rm b}$ given by the ratio of the moment of inertia of the white dwarf and the binary:

$$\frac{\Delta\dot{P}_{\rm b}}{\dot{P}_{\rm b}^{\rm GR}} \simeq \frac{I_{\rm WD}}{I_{\rm b}} = \frac{k}{q(q+1)}\left(\frac{R_{\rm WD}\sin i}{xc}\right)^2 = 1.2\times10^{-4}. \tag{14}$$

This means that, were the system synchronized, $\Delta\dot{P}_{\rm b}$ would be an insignificant correction given our current measurement precision.

If the white dwarf is not yet synchronized, then $\tau_s > \tau_c$. In this case $\Omega_{\rm WD}$ can be much larger than $2\pi/P_{\rm b}$, but it must still be smaller than the break-up angular velocity, i.e., $\Omega_{\rm WD} < (GM_{\rm WD}/R_{\rm WD}^3)^{1/2} = 0.0142\,{\rm rad\,s^{-1}}$. These conditions for $\Omega_{\rm WD}$ and τ_s yield $\dot{P}_{\rm b}^{\rm T} < 4.2\times10^{-16}\,{\rm s\,s^{-1}}$. Thus, even if the white dwarf were rotating near break-up velocity, $\dot{P}_{\rm b}^{\rm T}$ would still be two orders of magnitude smaller than the uncertainty in the measurement of $\dot{P}_{\rm b}$. We note, however, that the progenitor of the white dwarf was very likely synchronized with the orbit at formation, which had a period of $\sim$ 5 hours (see below). When the white dwarf formed, fall-back of material within the Roche lobe into it would have spun it up, but not by more than 1 order of magnitude (e.g., Appendix B2.2 of (*96*)). Therefore, at formation $\Omega_{\rm WD}$ was of the order of $3.5\times10^{-3}\,{\rm rad\,s^{-1}}$; this would yield $\dot{P}_{\rm b}^{\rm T} < 1.0\times10^{-16}\,{\rm s\,s^{-1}}$.

Constraints on dipolar radiation and Scalar-Tensor gravity In scalar-tensor gravity, like for most other alternatives to GR, the dominant contribution to the GW damping of the orbital

motion of a binary system would come from the scalar dipolar waves, proportional to $(\alpha_A - \alpha_B)^2$, where α_A and α_B denote the effective scalar-coupling constants of the two masses m_A and m_B, respectively, of the binary system. Such deviations should then become apparent as a modification in the orbital period decay observed in binary pulsars. In GR the emission of quadrupolar tensor waves enters the orbital dynamics at the 2.5 post-Newtonian (pN) level, which corresponds to corrections of order $(v/c)^5$ in the equations of motion, v being a typical orbital velocity. A contribution from dipolar GWs enters already at the 1.5pN level, i.e. terms of order $(v/c)^3$. As an example, in scalar-tensor gravity the change in angular orbital frequency $n_\mathrm{b} \equiv 2\pi/P_\mathrm{b}$ for a circular orbit caused by gravitational wave damping up to 2.5pN order is given by (*39, 97*)

$$\frac{\dot{n}_\mathrm{b}}{n_\mathrm{b}^2} = \frac{X_A X_B}{1+\alpha_A\alpha_B}\left[\frac{96}{5}\,\kappa\left(\frac{v}{c}\right)^5 + (\alpha_A-\alpha_B)^2\left(\frac{v}{c}\right)^3\right], \tag{15}$$

where

$$v \equiv [G_*(1+\alpha_A\alpha_B)(m_A+m_B)n_\mathrm{b}]^{1/3}\,, \tag{16}$$

with G_* denoting the bare gravitational constant, and $X_A \equiv m_A/(m_A+m_B)$ and $X_B \equiv m_B/(m_A+m_B)$. The quantity κ, where $\kappa = 1$ in GR, holds terms arising from the emission of scalar quadrupolar waves and higher order terms of the scalar dipolar emission (*39*):

$$\kappa = 1 + \frac{1}{6}\,(\alpha_A X_B + \alpha_B X_A)^2 + d_1\,(\alpha_A-\alpha_B) + d_2\,(\alpha_A-\alpha_B)^2 \tag{17}$$

and[3]

$$d_1 = \frac{1}{6}(\alpha_A X_A + \alpha_B X_B)(X_A - X_B) + \frac{5}{48}\,\frac{\beta_B\alpha_A X_A - \beta_A\alpha_B X_B}{1+\alpha_A\alpha_B}\,, \tag{18}$$

$$d_2 = \frac{5}{64} + \frac{253}{576}X_A X_B - \frac{39+49\,\alpha_A\alpha_B}{144(1+\alpha_A\alpha_B)} - \frac{5(X_B\alpha_B^2\beta_A + X_A\alpha_A^2\beta_B)}{72(1+\alpha_A\alpha_B)^2}\,. \tag{19}$$

GR is recovered for $G_* = G$ and $\alpha_A = \alpha_B = 0$. Equation (15) can directly be confronted with the results compiled in Table 1, in combination with the p.d.f. of the white dwarf mass in Fig. 3, where we use index A for the pulsar and index B for the white dwarf companion.[4] One finds from the mass ratio q that $X_A = q/(q+1) = 0.9213 \pm 0.0008$ and $X_B = 1/(q+1) = 0.0787 \pm 0.0008$. Furthermore, since $G_*(m_A+m_B) \simeq G m_B(q+1)$, one has $v/c = (0.001970 \pm 0.000016)\times(1+\alpha_A\alpha_B)^{1/3}$. With the observed change in the orbital frequency $\dot{n}_\mathrm{b} = -2\pi\dot{P}_\mathrm{b}/P_\mathrm{b}^2 = (2.23\pm0.36)\times10^{-20}$, which agrees with GR, one can infer the following constraint on $(\alpha_A - \alpha_0)$ using equation (15):

$$|\alpha_A - \alpha_0| < 0.005 \quad (95\%\ \mathrm{C.L.})\,. \tag{20}$$

[3]To our knowledge, the quantity d_2 has been calculated here for the first time.

[4]Strictly speaking, when using the masses of Table 1 in equation (15) one has to keep in mind the difference between the bare gravitational constant G_* and Newton's gravitational constant $G = G_*(1+\alpha_0)^2$ as measured in a Cavendish-type experiment. However, since $\alpha_0^2 < 10^{-5}$, we can ignore this difference in our calculations.

Our detailed calculations show that this limit is solely enforced by the dominant 1.5pN term of equation (15) (see also equation (1) in the main text), and is practically insensitive to the values assumed by β_A and β_B. Consequently, as in (*23, 98*) the limit (20) can be seen as a generic limit, that is independent of the EOS.

To illustrate how PSR J0348+0432 probes a new gravity regime, we present detailed calculations based on a specific EOS and a specific class of alternative gravity theories. As an EOS we use the rather stiff EOS ".20" of (*27*), which supports (in GR) neutron stars of up to $2.6\,\mathrm{M}_\odot$. Concerning the alternative gravity theories, we use the class of "quadratic" mono-scalar-tensor theories used in (*3, 4*), where the (field-dependent) coupling strength $\alpha(\varphi)$ between the scalar field and matter contains two parameters: $\alpha(\varphi) = \alpha_0 + \beta_0\varphi$. Every pair (α_0, β_0) represents a specific scalar-tensor theory of gravity. As discovered in (*3*), for certain values of β_0, neutron stars can develop a significant scalarization, even for vanishingly small α_0, if their mass exceeds a critical (β_0-dependent) value. For this reason, this class of gravity theories is particularly well suited to demonstrate how the limit (20) probes a new gravity regime that has not been tested before (see Fig. 2b). The specific parameters and EOS in Fig. 2b have been chosen for demonstration purposes. A change in the EOS, for instance, would lead to a modification in the details of the functional shape of α_A, but would not change the overall picture.

Constraints on the phase evolution of neutron-star mergers So far, the best constraints on dipolar gravitational wave damping in compact binaries come from the observations of the millisecond pulsar PSR J1738+0333, a $1.47^{+0.07}_{-0.06}\,\mathrm{M}_\odot$ neutron star in a tight orbit ($P_\mathrm{b} \approx 8.5\,\mathrm{h}$) with a spectroscopically resolved white-dwarf companion (*14, 23*). However, as discussed in detail above, such timing experiments are insensitive to strong-field effects that might only become relevant in the strong gravitational fields of high-mass neutron stars. Consequently, the dynamics of a merger of a $2\,\mathrm{M}_\odot$ neutron star with a "canonical" neutron star or a black hole (BH) might have a significant contribution from dipolar GW damping, leading to a modification of the orbital dynamics that is incompatible with the sophisticated GR templates used to search for GWs with ground-based GW detectors, like LIGO and VIRGO, (*34*). With the results on PSR J0348+0432, in particular with the limit given in eq. (20), this question can finally be addressed in some details. For this purpose, we decompose equation (15) into the 2.5pN contribution, that is matched by an appropriate GR template, and the 1.5pN contribution, that drives the phase evolution away from the 2.5pN dynamics. Following (*38, 39*), we introduce the dimensionless orbital angular velocity

$$u \equiv \mathcal{M} n_\mathrm{b} = \pi \mathcal{M} f_\mathrm{GW} \,, \tag{21}$$

where f_GW denotes the frequency of the GW and

$$\mathcal{M} \equiv \frac{G_* M}{c^3} \frac{(X_A X_B \kappa)^{3/5}}{(1+\alpha_A\alpha_B)^{2/5}} \,. \tag{22}$$

To leading order, one then finds

$$\mathcal{M}\dot{u} = \frac{96}{5}(u^{11/3} + \mathcal{B}u^3) \,, \tag{23}$$

where

$$\mathcal{B} \equiv \frac{5}{96}\left(\frac{X_A X_B}{1+\alpha_A\alpha_B}\right)^{2/5}\frac{(\alpha_A-\alpha_B)^2}{\kappa^{3/5}}\ . \tag{24}$$

The observed GW cycles in a frequency band $[f_{\rm in}, f_{\rm out}]$ can be computed as follows:

$$N_{\rm GW} = \int_{t_{\rm in}}^{t_{\rm out}} f\,dt = \int_{f_{\rm in}}^{f_{\rm out}} (f/\dot{f})\,df = \frac{1}{\pi}\int_{u_{\rm in}}^{u_{\rm out}} \frac{u}{\mathcal{M}\dot{u}}\,du\ . \tag{25}$$

Consequently, the difference between the 2.5pN dynamics and the 2.5pN + 1.5pN dynamics is given by

$$\Delta N_{\rm GW} = \frac{5}{32\pi}\left(\frac{1}{5u^{5/3}} - \frac{1}{3u\mathcal{B}} + \frac{1}{u^{1/3}\mathcal{B}^2} + \frac{\arctan\left(u^{1/3}/\mathcal{B}^{1/2}\right)}{\mathcal{B}^{5/2}}\right)\Bigg|_{u_{\rm in}}^{u_{\rm out}}\ , \tag{26}$$

where we made no assumption about the size of the value for $\mathcal{B}$. For the LIGO/VIRGO band $u_{\rm in} \ll u_{\rm out}$.[5] Fig. 5 gives $\Delta N_{\rm GW}$ for the LIGO/VIRGO detectors, for which a typical bandwidth of 20 Hz to a few kHz was assumed, as a function of $|\alpha_A - \alpha_0|$ for two different systems, a $2/1.25\,{\rm M}_\odot$ NS-NS system and a $2/10\,{\rm M}_\odot$ NS-BH system. Concerning the NS-BH systems, we considered the class of alternative gravity theories where BHs are practically identical to GR, and consequently used $\alpha_B = 0$. For instance, this is the case in scalar-tensor gravity theories with negligible time dependence of the asymptotic scalar field (*39*). For the NS-NS system an extreme case is represented by the assumption that only the massive neutron star has a significant scalar coupling strength α_A, while the lighter companion behaves like a weakly self-gravitating body, meaning $\alpha_B = \alpha_0$. Besides this, for the NS-NS system we have also performed calculations using a hypothetical most conservative (maximal $\Delta N_{\rm GW}$) value for the effective coupling strength of the companion B, which is $\alpha_B = 0$. However, such an assumption seems unphysical for a non-zero α_0, where α_B is expected to approach α_0 (and not 0) for less massive stars. With the limit obtained from PSR J0348+0432 we find a conservative upper limit for the dipolar phase offset of ~ 0.5 (NS-NS) and 0.04 (NS-BH) cycles, an amount that would not jeopardize the detection of the gravitational wave signal in the LIGO/VIRGO band (*37*).

Formation via a common envelope and spiral-in phase Common-Envelope (CE) evolution (*40,99*) in X-ray binaries is initiated by dynamically unstable mass transfer, often as the result of a high mass-transfer rate and a large initial donor/accretor mass ratio, $q_{\rm i} \equiv M_2/M_{\rm PSR} > 1$. If the CE is initiated while the donor star is still early in its main sequence stage (i.e. if $P_{\rm b} < 1$ day), the outcome is expected to be a merger (*100*). It is generally believed that a binary can only survive the CE evolution, and thereby successfully eject the envelope of the donor star, if the binding energy of the envelope, $E_{\rm bind}$, is less than the released orbital energy from the in-spiral process,

[5]For a detector that is sensitive up to a few kHz, the frequency $f_{\rm GW}^{\rm out}$ is determined by the innermost circular orbit, which is ~ 1350 Hz for a $2/1.25\,{\rm M}_\odot$ system and ~ 370 Hz for a $2/10\,{\rm M}_\odot$ system (see (*35*)).

$\Delta E_{\rm orb}$ (*101*). The orbital energy of PSR J0348+0432 is: $|E_{\rm orb}| = GM_{\rm PSR}M_{\rm WD}/2a \simeq 5.5{\times}10^{47}$ erg. Hence, even if assuming in-spiral from infinity to the current orbital separation, the amount of liberated orbital energy from the CE phase cannot exceed this value. From calculations of $E_{\rm bind}$ of intermediate-mass stars (Table S3), we find that $E_{\rm bind} \gg \Delta E_{\rm orb}$ during most of their evolutionary stages. Only if the donor star (i.e. the white dwarf progenitor) is an evolved giant is it possible to eject the envelope. However, in this case the core mass of such an evolved star, $M_{\rm core}$, is more massive than the observed white dwarf companion by at least a factor of $2-3$. (As argued in the main text, a reduction in white dwarf mass via evaporation from the pulsar wind seems to be ruled out for PSR J0348+0432 and therefore cannot help circumvent this discrepancy.)

From Fig. 7 we see that only a low-mass donor star with mass $M_2 \leq 2.2\,{\rm M}_\odot$, and not evolved beyond the terminal age main-sequence (TAMS), would leave behind $M_{\rm core} = M_{\rm WD} \simeq 0.17\,{\rm M}_\odot$. In this case, it is clear that energy sources other than $\Delta E_{\rm orb}$ must contribute to expel the envelope (since in this case $E_{\rm bind} \gg \Delta E_{\rm orb}$). Such an energy source could be the release of gravitational potential energy from material which accretes onto the neutron star during the CE. The amount of released energy per accreted unit mass is roughly $\Delta U/m \sim GM/R \sim 2 \times 10^{20}\,{\rm erg\,g^{-1}}$. Hence, assuming full absorption and 100% energy conversion of this released energy to eject the envelope, this would require accretion of $\sim 4 \times 10^{-5}\,{\rm M}_\odot$; a value which is not unrealistic given a timescale of the CE event of $\sim 10^3$ yr with Eddington limited accretion (a few $10^{-8}\,{\rm M}_\odot\,{\rm yr^{-1}}$).

As a consequence of this relatively short CE phase, the currently observed mass of $M_{\rm PSR} = 2.01\,{\rm M}_\odot$ should be close to the original mass of the neutron star after its formation in a type Ib/c supernova. According to recent studies by (*102*), neutron star birth masses of $2.0\,{\rm M}_\odot$ are indeed possible. As mentioned in the main text, however, having an initially massive neutron star would be a more serious problem for formation via a CE event with a $\leq 2.2\,{\rm M}_\odot$ donor star. Such a high value of $M_{\rm PSR}$ would lead to a value of $q_{\rm i}$ close to unity, in which case the Roche-lobe overflow (RLO) is expected to be dynamically *stable*, thereby avoiding the formation of a CE (*42, 43*). The only solution to this problem would be that the neutron star was originally born with a more typical mass of $\sim 1.4\ M_\odot$, in which case $q_{\rm i}$ would be sufficiently high to ensure formation of a CE. However, in that case one would have to accept the concept of hypercritical accretion (*46, 103*), allowing the neutron star to accrete a large amount of mass $\sim 0.5-0.7\,{\rm M}_\odot$ on a timescale of $\sim 10^3$ yr. One could argue that PSR J0348+0432 would then be the best (and to our knowledge the only) candidate known in which hypercritical accretion might have been at work.

To summarize, given the many issues discussed above we find that a CE formation channel is less favorable to explain PSR J0348+0432 and we now proceed with investigating another solution, the LMXB formation channel.

Formation via a converging low-mass X-ray binary As mentioned in the main text, a handful of binary pulsars exist with values of $P_{\rm b} \leq 8$ hr and $M_{\rm WD} \approx 0.14-0.18\,{\rm M}_\odot$, similar to those of PSR J0348+0432. These systems are tentatively thought to descend from low-mass X-ray

binaries (LMXBs) in which the binary suffered from loss of orbital angular momentum caused by magnetic braking (*43, 47, 48*). However, there remains a general problem for reproducing these pulsar binaries using current stellar evolution codes. A main issue is that converging LMXBs most often do not detach but keep evolving with continuous mass transfer to more and more compact systems with $P_{\rm b} \leq 1\,{\rm hr}$ and ultra-light donor masses $M_2 < 0.08\,{\rm M}_\odot$. In a few instances, where fine-tuning may lead to detachment and the right values of $P_{\rm b}$ and M_2, the donor star is typically too hydrogen rich to settle and cool as a compact He white dwarf [however, see sequence *d* in fig. 16 of (*43*) for an exception]. Our numerical studies are no exception from this general picture.

Using the Langer stellar evolution code [e.g. (*41, 104*)] we have attempted to model the formation and evolution of the PSR J0348+0432 system. Here we present a solution where we have forced the donor star to detach its Roche lobe at $P_{\rm b} \sim 5\,{\rm hr}$, such that the system subsequently shrinks in size to its present value of $P_{\rm orb} \simeq 2.46\,{\rm hr}$ due to GW radiation within the estimated cooling age of the white dwarf ($t_{\rm WD} \simeq 2\,{\rm Gyr}$, depending on cooling models and assumed metallicity). To be more precise, the estimated $t_{\rm WD}$ is actually a lower limit on the timescale during which the detached system evolved via GW radiation since it takes $10^8 - 10^9\,{\rm yr}$ for the detached pre-white dwarf to settle on the final cooling track. This can be compensated for by choosing a slightly larger $P_{\rm b}$ at the ZAMS, which causes the system to detach from the LMXB in a somewhat wider orbit.

In Fig. 8 (and see also Fig. 6 in the main text) we show an example of our LMXB calculations. The model binary shown here consisted initially of a $1.75\,{\rm M}_\odot$ neutron star and a $1.1\,{\rm M}_\odot$ donor star with metallicity $Z = 0.02$, mixing length parameter, $\alpha = 2.0$ and ZAMS orbital period, $P_{\rm b} = 2.55\,{\rm days}$. The initial $P_{\rm b}$ depends on the modeling of magnetic braking. Here the value corresponds to onset of RLO at $P_{\rm b} \simeq 0.65\,{\rm days}$, shortly after the donor star ceased central hydrogen burning. Our high value of the initial neutron star mass is motivated from studies which show that the accretion efficiency in LMXBs must be rather small — even for systems which are expected to have accreted at sub-Eddington levels (*14, 15, 42*). Hence, by adopting an accretion efficiency of only 30% we need an initial high-mass neutron star in order to reach the present mass of PSR J0348+0432. Note, that some neutron stars are indeed expected to have been born massive [for a discussion, see (*41*) and references therein]. The outcome of our calculations would possibly have been somewhat similar by assuming an accretion efficiency close to 100% and starting with $M_{\rm PSR} = 1.3\,{\rm M}_\odot$. To model the loss of orbital angular momentum due to mass loss from the system, we adopted the isotropic re-emission model (*105*).

Based on its proper motion and radial velocity measurements, PSR J0348+0432 has an estimated 3D space velocity of $56 \pm 8\,{\rm km\,s^{-1}}$ with respect to the Solar System. From Monte Carlo simulations of its past motion through our Galaxy [following the method described in (*14, 106*)], we find that this velocity corresponds to a peculiar velocity with respect to the local standard of rest at every transition of the Galactic plane of $75 \pm 6\,{\rm km\,s^{-1}}$. This result is rather independent of the applied Galactic model. From subsequent simulations of the dynamical effects of the supernova explosion, we find that a relatively small kick magnitude of $w < 150\,{\rm km\,s^{-1}}$ was imparted to the newborn neutron star, by probing a broad range of values of the pre-supernova

orbital period and the masses of the collapsing naked He-core and its companion star (the white dwarf progenitor).

Spin evolution of PSR J0348+0432 A peculiarity of PSR J0348+0432, compared to other recycled pulsars with similar $P_{\rm b}$ and $M_{\rm WD}$, is its slow spin period, $P = 39$ ms and its high value of the spin period derivative, $\dot{P} = 2.41 \times 10^{-19}$ s s^{-1}, cf. the unusual location of PSR J0348+0432 in both the $P\dot{P}$-diagram and the Corbet-diagram (Figs. S9, S10). In particular, the Corbet diagram clearly displays the unique characteristics of PSR J0348+0432 with a small $P_{\rm b}$ and a large value of P.

During the LMXB phase, a pulsar is generally expected to accrete much more mass and angular momentum than needed to be spun-up to a few milliseconds (*49*). In the same process, its B-field should have decayed significantly — typically to values $\leq 10^8$ G. However, for some reason the B-field ($\sim 2 \times 10^9$ G) remained relatively high in PSR J0348+0432. In contrast, the other known binary radio pulsars with similar values of $P_{\rm b} \leq 8$ hr and $M_{\rm WD} \approx 0.14 - 0.18\,{\rm M}_\odot$ (e.g. PSRs J0751+1807 and J1738+0333), besides from the many black-widow-like systems, have low B-fields and spin periods of a few milliseconds, as expected from current theories of LMXB evolution.

In Fig. 11 we have plotted the past and the future evolution of PSR J0348+0432. In the upper panel is seen the evolution of $P_{\rm b}$. In the lower panel is seen the spin evolution of the pulsar assuming different values of a constant braking index $2 \leq n \leq 5$. If the estimated cooling age of ~ 2 Gyr is correct (and adding to this value a pre-white dwarf contraction phase between RLO detachment and settling on the final cooling track, yielding an assumed total age of about $2 - 2.5$ Gyr) we can estimate that PSR J0348+0432 was recycled with an initial spin period of about $10 - 20$ ms. This relatively slow spin could be (partly) caused by enhanced braking of the spin rate, due to the high B-field of the pulsar, during the Roche-lobe decoupling phase when the progenitor of the white dwarf ceased its mass transfer (*50*). If the total post-LMXB age is ~ 2.6 Gyr then the pulsar could, at first sight, have been recycled with an initial spin period of 1 ms for $n \geq 3$. However, calculations of the pulsar spin-up line (*49*) do not predict such a rapid spin for pulsars with high B-fields and which accreted with typical mass-accretion rates of $\dot{M} < 10^{-2}\,\dot{M}_{\rm Edd}$ (evident from both theoretical modeling of the LMXB RLO and observations of LMXB luminosities (*107*)).

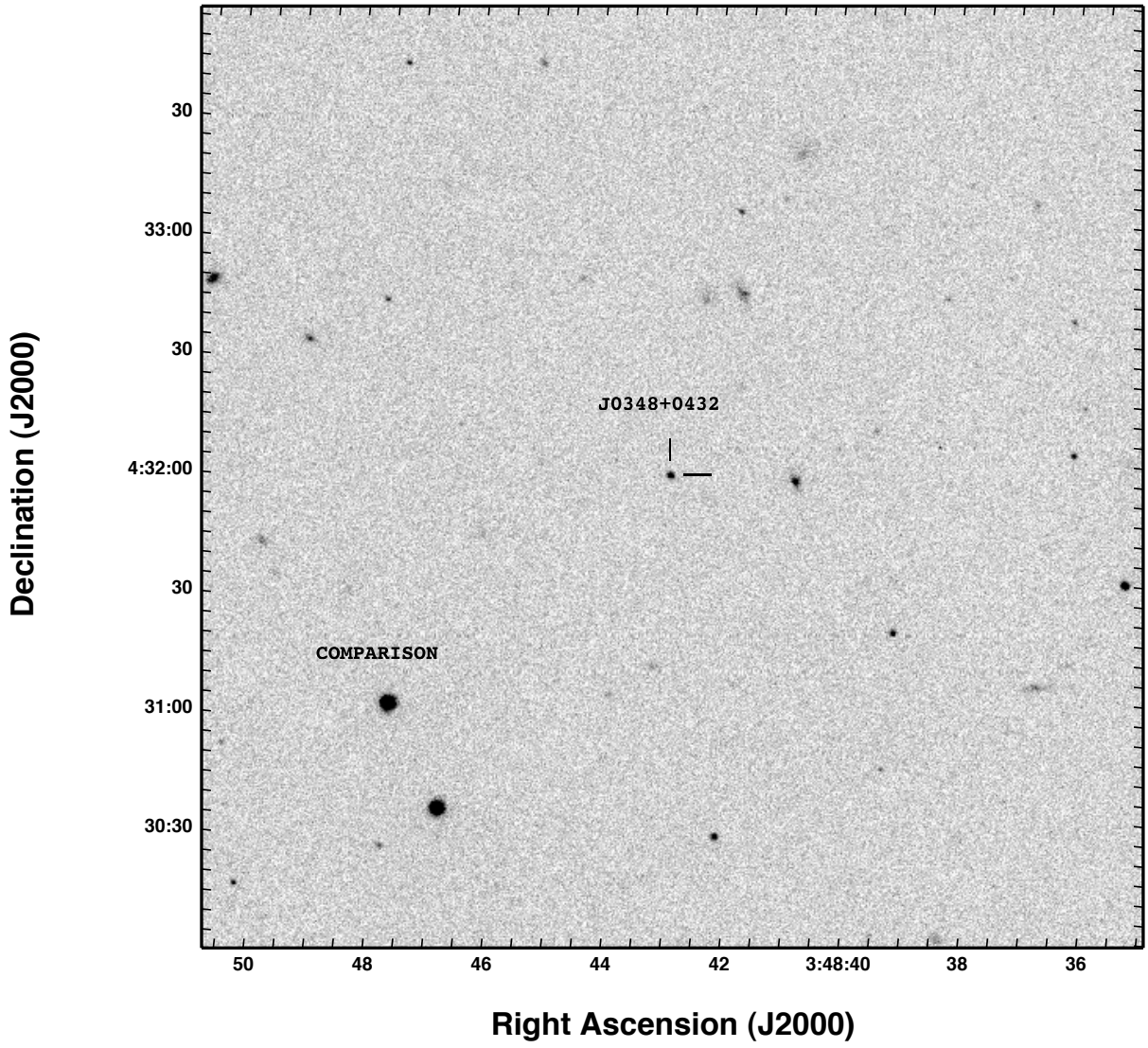

Figure 1: Finding chart for the PSR J0348+0432 system and the comparison star used in our analysis (see text), created from the archived SDSS g' image.

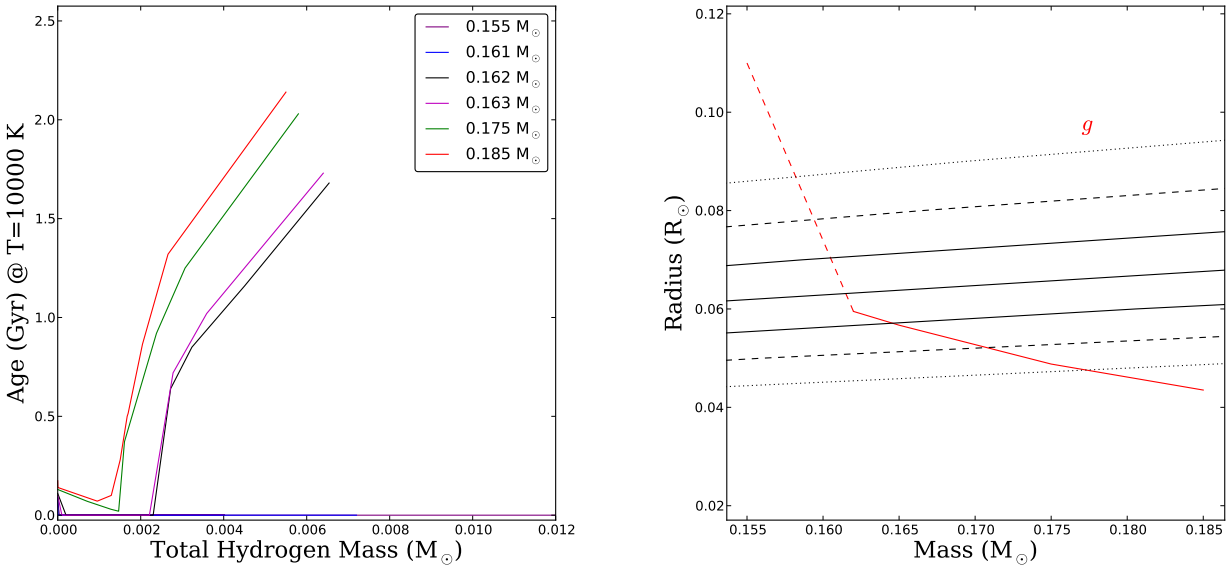

Figure 2: **Left:** White dwarf cooling age (measured from the onset of the core contraction) when the temperature reaches $T_{\rm eff} = 10000$ K as a function of the total hydrogen mass of the star. Each line depicts a different total mass (from 0.155 to 0.185 $M_\odot$). For each model, hydrogen burning through the pp-chain at the bottom of the stellar envelope cannot be initiated below a critical envelope mass limit. As a result the white dwarf cools in a few Myr. For models below $\sim 0.162\,M_\odot$ a temperature of 10000 K cannot be reached regardless of the envelope size. **Right:** Finite-temperature mass-radius relation (for 10000 K) for models that have the minimum envelope mass required for hydrogen burning (red line). Over-plotted are the most-likely value and 1, 2 and 3σ constraints on the surface gravity for PSR J0348+0432 (solid, dashed and dotted black lines respectively). For masses below $0.162\,M_\odot$ the radius is an extrapolation from lower temperatures (in dashed red).

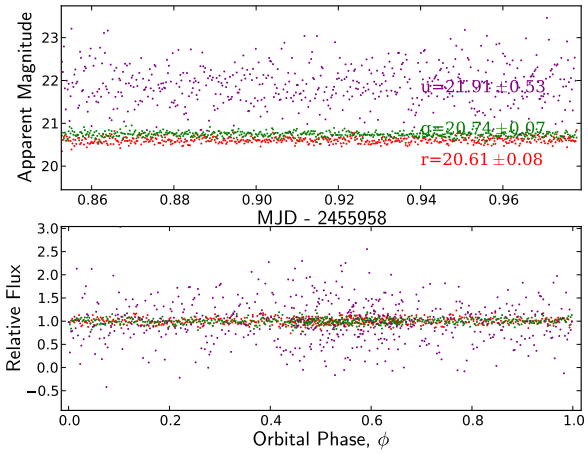

Figure 3: Photometric (upper) and phase-folded (lower) light-curve of the white dwarf companion to PSR J0348+0432 in u', g' and r'.

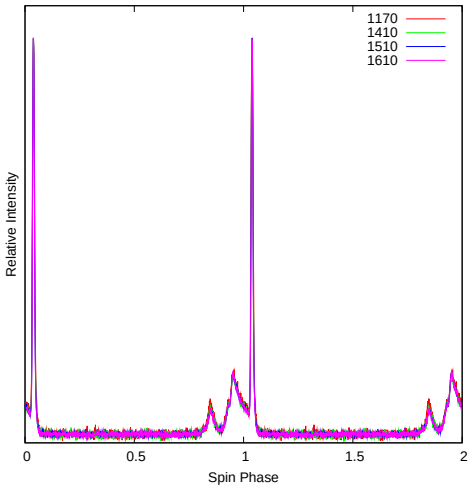

Figure 4: Pulse profiles for PSR J0348+0432 obtained with the WAPP spectrometers at frequencies of 1170, 1410, 1510 and 1610 MHz. Two full cycles are displayed for clarity. Their (almost) perfect overlap indicates that there is little pulse profile evolution between 1170 and 1610 MHz. The 1410 MHz pulse profile is the template used to derive all TOAs. The TOAs correspond to integer phases in this plot, which mark the maximum of the fundamental harmonic.

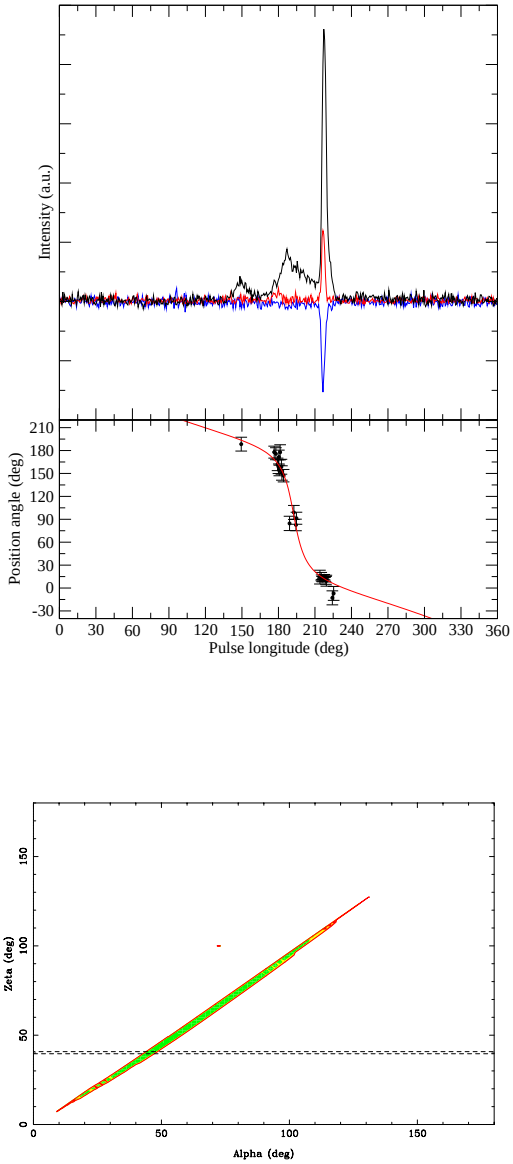

Figure 5: **Top:** Polarization profile of PSR J0348+0432 obtained with the Effelsberg Telescope. The upper panel shows total intensity (I, black), the linearly polarized intensity (L, red) and the circularly polarized intensity (V, blue). The lower panel shows the position angle of L measured at pulse longitudes where L exceeds 2σ measured from an off-pulse RMS. The red line shows the resulting fit of a Rotating Vector Model (RVM), which indicates an "outer line-of-sight" (see (*82*) for details). **Bottom:** Map of the RVM parameters α (the angle between the spin axis and magnetic axis) and ζ (the angle between the line of sight and the spin axis). The green region corresponds to combinations of α, ζ for which the RVM provides a good description of the polarimetry of PSR J0348+0432. Based on the polarimetry alone we would have a large uncertainty regarding α and ζ. However, if we assume that during the accretion episode that recycled the pulsar the spin axis of the pulsar was aligned with the orbital angular momentum (which has an angle $i = 40.^{\circ}2 \pm 0.^{\circ}6$ to the line of sight) then $\alpha \simeq 45^{\circ}$. The minimum angle between the magnetic axis and the line of sight is then given by $\beta = \zeta - \alpha = -4.^{\circ}8$.

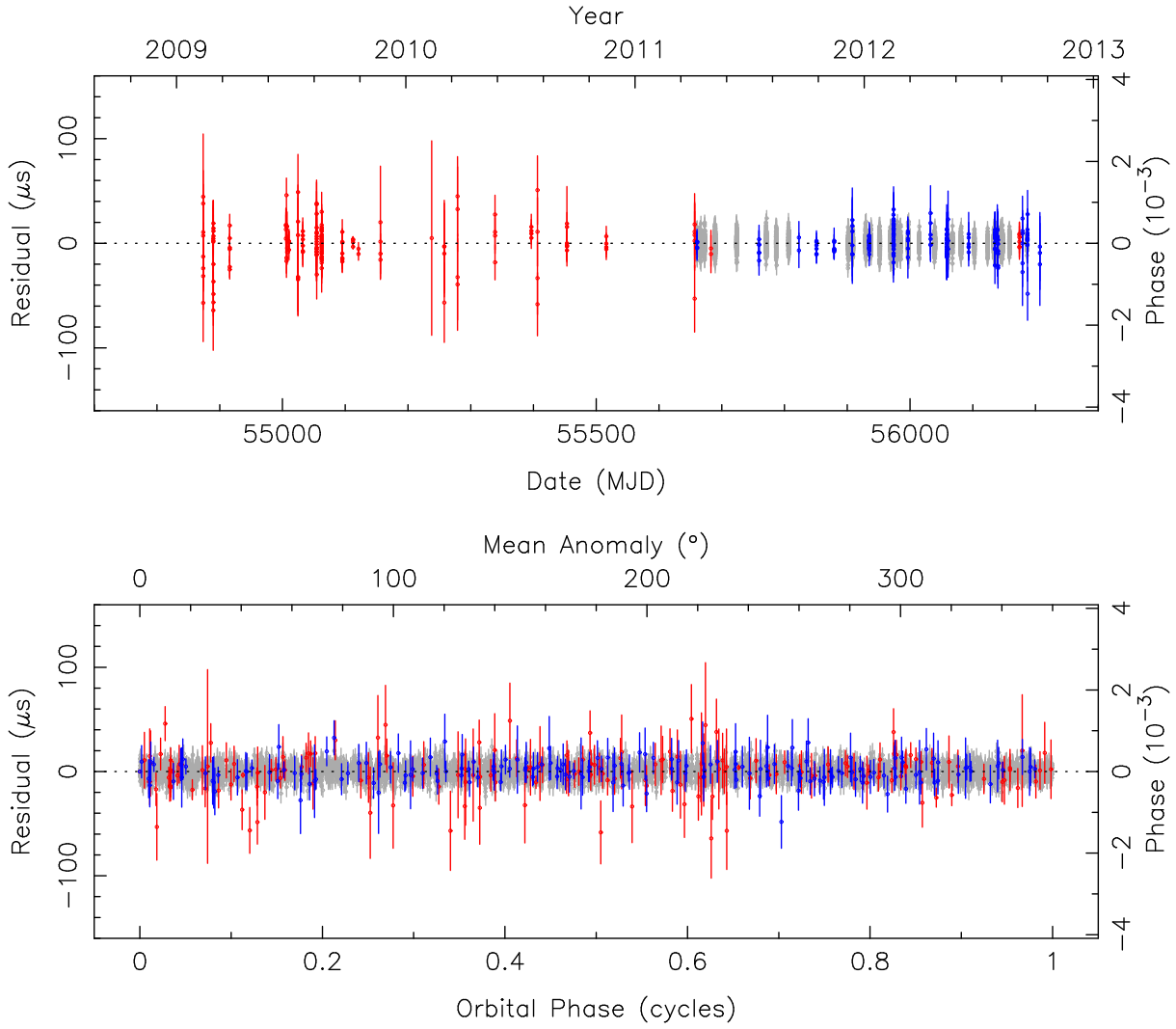

Figure 6: Post-fit residuals from the GBT (red), Arecibo (gray) and Effelsberg (blue) TOAs, obtained with the timing model presented in Table 1. **Top:** Residuals versus time. No significant un-modeled trends can be found in the TOA residuals. **Bottom:** Post-fit residuals versus orbital phase, which for this very low-eccentricity system is measured from the ascending node (i.e., the mean anomaly is equal to the orbital longitude). No significant trends can be identified in the residuals; indicating that the orbital model can describe the orbital modulation of the TOAs correctly. No dispersive delays or unaccounted Shapiro delay signatures are detectable near orbital phase 0.25 (superior conjunction), nor artifacts caused by incorrect de-dispersion or folding of the data.

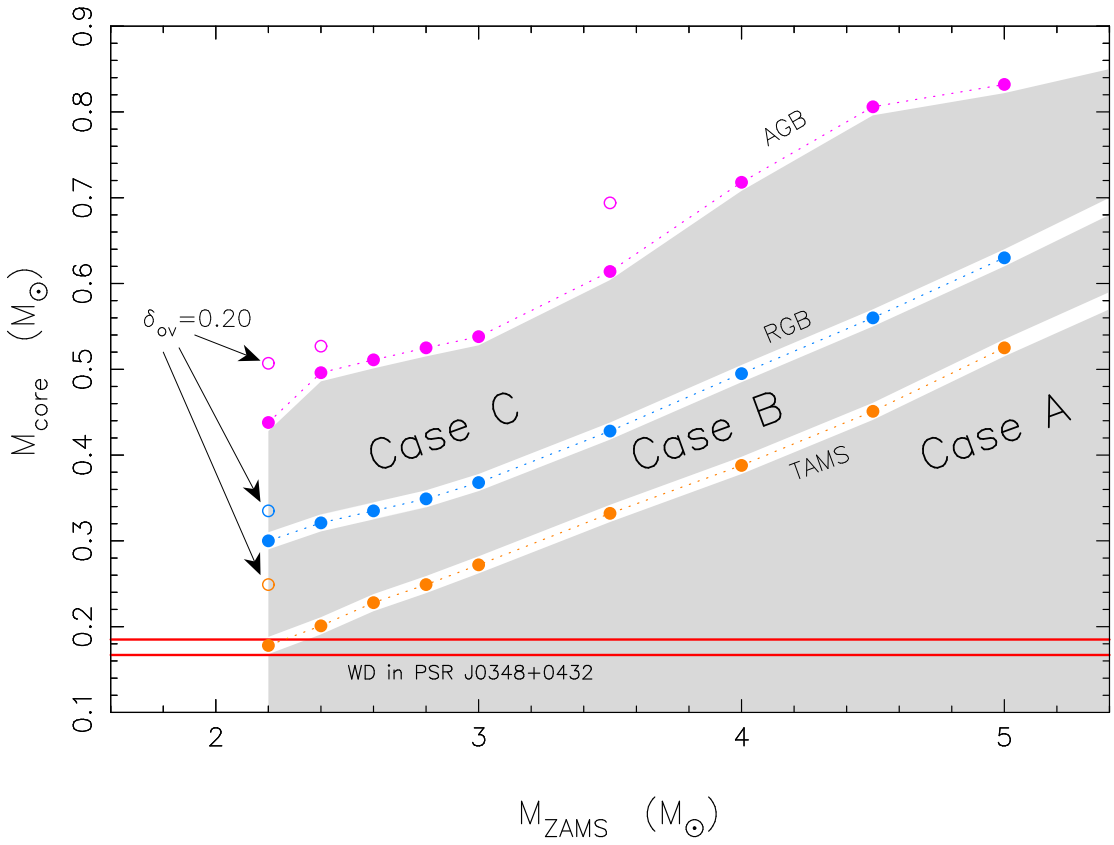

Figure 7: Stellar core mass at different evolutionary epochs as a function of zero-age main sequence (ZAMS) mass. Assuming $M_{\rm core} = M_{\rm WD} \simeq 0.17\,{\rm M}_\odot$ (as observed in PSR J0348+0432) constrains the progenitor star ZAMS mass to be $\leq 2.2\,{\rm M}_\odot$ and that its envelope was lost near the terminal-age main sequence (TAMS). All calculations were performed without convective core overshooting. Including this effect (for example, using $\delta_{\rm OV} = 0.20$) would lower the required donor mass even more. [Figure adapted from (*41*)].

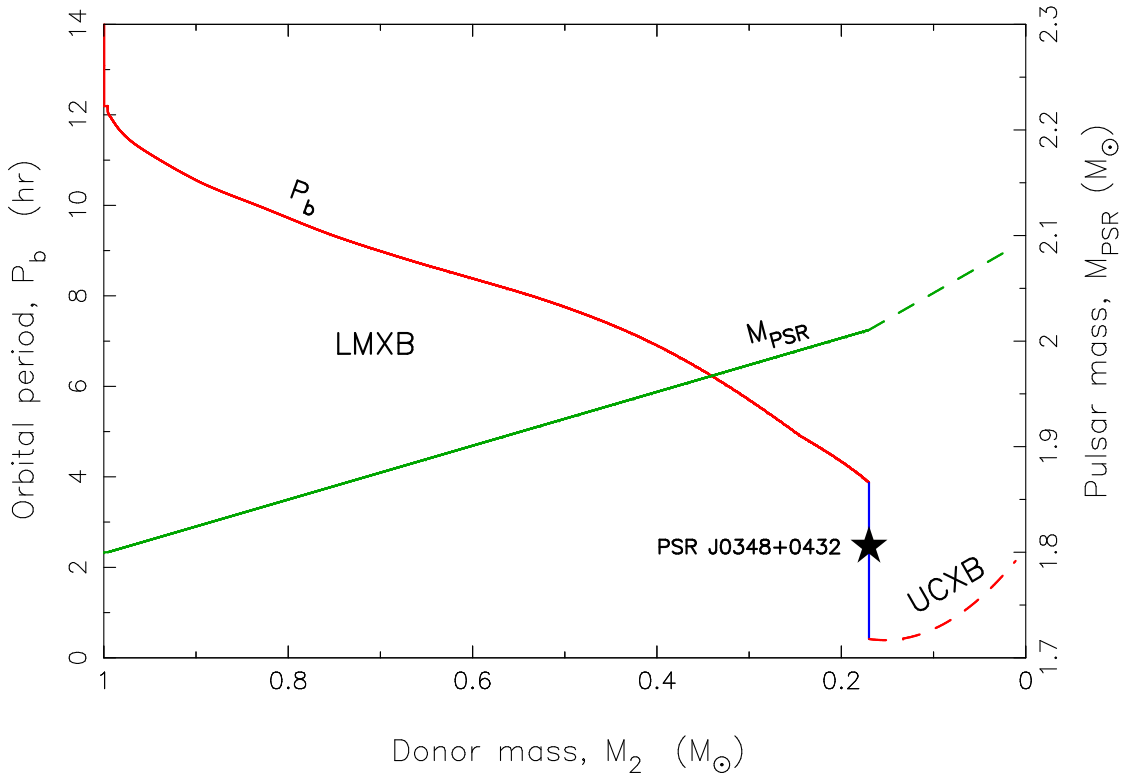

Figure 8: Formation of PSR J0348+0432 from a converging LMXB for the same model as shown in Fig. 6 in the main text. The plot shows how P_b (red line) and the mass of the accreting neutron star (green line) evolved as a function of decreasing donor star mass (here assumed to be 1.1 $M_\odot$ on the ZAMS). The RLO was initiated when $P_b \simeq 16$ hr and detached when $P_b \simeq 4.9$ hr. In this model the initial mass of the neutron star was assumed to be 1.75 $M_\odot$, although it may have been significantly lower if the neutron star accreted with an efficiency close to 100%. The present location of PSR J0348+0432 is marked with a star.

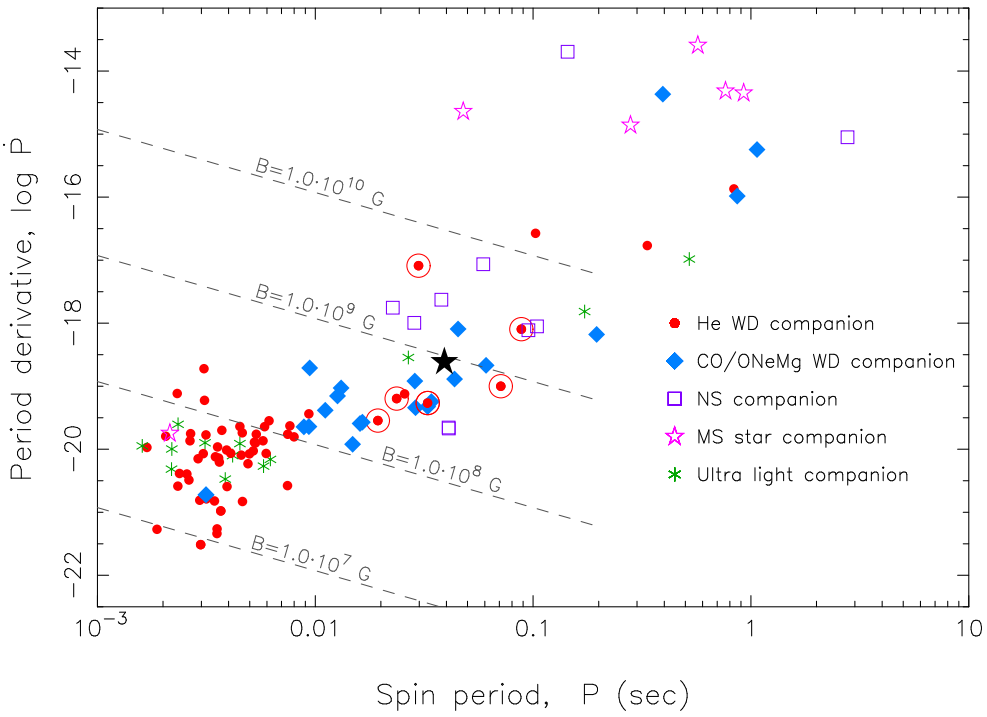

Figure 9: A $P\dot{P}$–diagram of the 111 known binary radio pulsars in the Galactic disk. The location of PSR J0348+0432 is marked with a black star in a region which is mainly dominated by slow spin and high B-field pulsars with massive white dwarf companions (marked with blue diamonds). The dashed lines of constant B-fields were calculated following (*49*) and assuming for simplicity $M_{\rm PSR} = 1.4\ {\rm M}_\odot$ and $\sin\alpha = \phi = \omega_{\rm c} = 1$. All $\dot{P}$ values in this plot are intrinsic values obtained from kinematic corrections to the observed values. Data taken from the ATNF Pulsar Catalogue (*108*), in Oct. 2012.

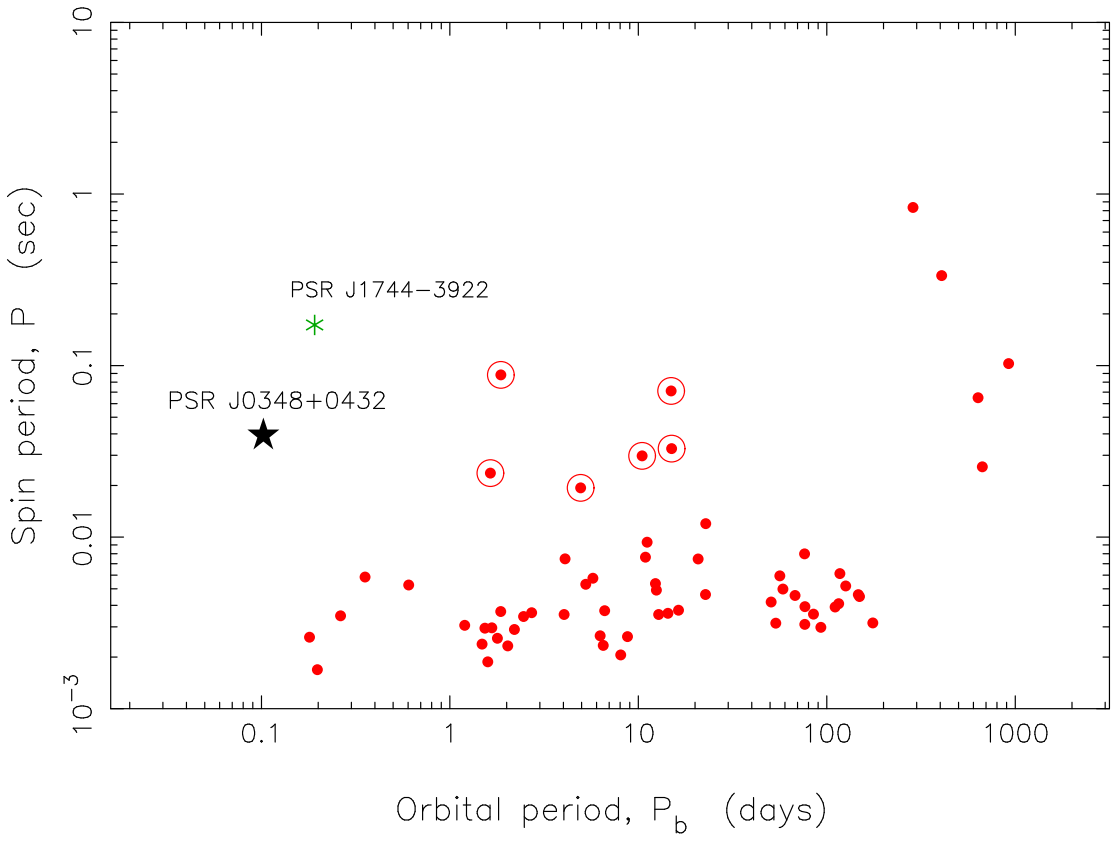

Figure 10: A $P_{\rm b} - P$ (Corbet) diagram of the 63 known Galactic binary pulsars with a He white dwarf companion of mass $M_{\rm WD} > 0.14\,{\rm M}_{\odot}$. The unique location of PSR J0348+0432 is shown with a star. Another puzzling pulsar, PSR J1744−3922 (*45*) marked with a green asterisk, is included in this plot. These two pulsars seem to share high B-field properties with the 6 pulsars in circles. Data taken from the ATNF Pulsar Catalogue (*108*), in Sep. 2012.

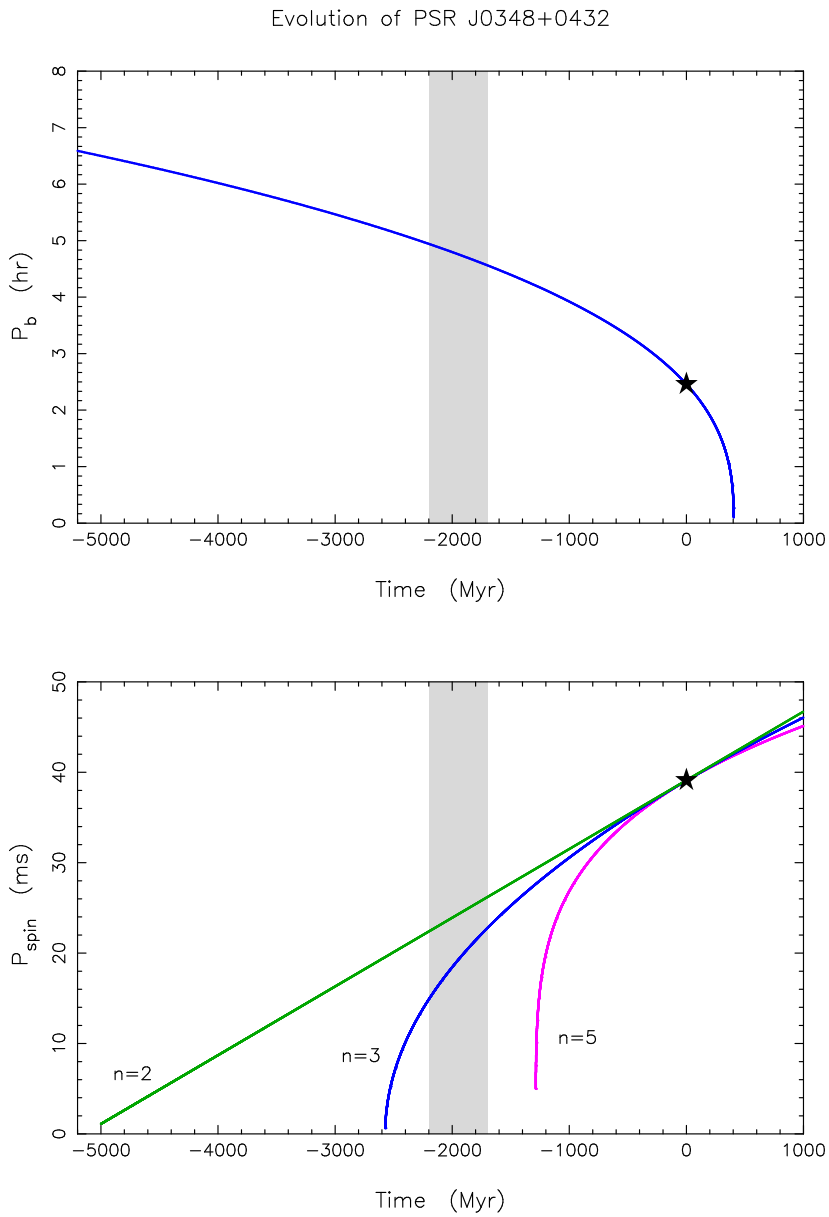

Figure 11: Orbital evolution (top) and spin evolution (bottom) of PSR J0348+0432 in the past and in the future. Different evolution tracks are plotted for different assumed values of a (constant) braking index, n. The grey shaded region marks the estimated white dwarf cooling age. The past is for a negative value of time, future is for a positive value of time. See text for a discussion.

Table 1: Observations log and radial velocity measurements

Notes: (1) refers to the barycentric mid-exposure time. (2) is the orbital phase, ϕ, using the ephemeris in Table 1. (3) is the comparison's velocity in respect to the Solar System Barycenter and (4) the raw barycentric velocities of the white dwarf companion to PSR J0348+0432.

Target	No.	MJD^{1}_{bar}	ϕ^{2}	slit	exposure s	rotation deg	pos. angle deg	v^{3}_{R} (km s^{-1})	v^{4}_{WD} (km s^{-1})
PSR J0348+0432	1	55915.070159	0.9742	1″	799.96	−135.0	−150.0	−18.24 ± 0.41	−348.25 ± 7.17
	2	55915.080011	0.0704	1″	799.96	−135.0	−155.1	−22.46 ± 0.39	−345.54 ± 7.55
	3	55915.099359	0.2593	1″	799.95	−135.0	−166.5	−29.37 ± 0.40	−12.36 ± 9.71
	4	55915.109036	0.3538	1″	799.96	−135.0	−172.8	−25.21 ± 0.39	+159.76 ± 9.54
	5	55915.120877	0.4694	1″	799.96	−135.0	+179.2	−19.26 ± 0.38	+332.63 ± 8.37
	6	55915.130692	0.5652	1″	799.98	−135.0	+172.7	−20.79 ± 0.38	+295.18 ± 8.08
	7	55915.140364	0.6596	1″	799.97	−135.0	+166.4	−19.54 ± 0.38	+149.72 ± 8.77
	8	55915.150194	0.7556	1″	799.98	−135.0	+160.4	−19.41 ± 0.38	−45.85 ± 8.76
	9	55915.217387	0.4116	1″	799.96	−134.8	+132.1	−8.28 ± 0.44	+311.34 ± 11.94
	10	55915.227349	0.5089	1″	849.96	−134.8	+129.7	−9.74 ± 0.43	+360.61 ± 11.87
	11	55915.237602	0.6090	1″	849.97	−134.8	+127.3	−5.13 ± 0.44	+278.11 ± 11.03
	12	55915.247859	0.7092	1″	849.95	−134.8	+125.4	−4.85 ± 0.46	+86.48 ± 13.56
	13	55915.261379	0.8412	1″	799.96	−134.8	+123.1	−3.10 ± 0.42	−143.98 ± 13.42
	14	55915.271051	0.9356	1″	799.97	−134.8	+121.7	−2.20 ± 0.46	−297.87 ± 14.87
	15	55915.280729	0.0301	1″	799.96	−134.8	+120.4	−0.34 ± 0.52	−272.12 ± 18.87
	16	55915.290404	0.1245	1″	799.97	−134.8	+119.5	+1.56 ± 0.61	−188.66 ± 33.02
	17	55916.060700	0.6452	1″	799.98	−134.8	−146.8	−49.62 ± 0.44	+197.14 ± 15.88
	18	55916.070535	0.7412	1″	799.97	−134.8	−151.6	−52.40 ± 0.50	−10.28 ± 21.58
	19	55916.080364	0.8372	1″	799.96	−134.8	−156.8	−50.10 ± 0.51	−209.03 ± 20.37
	20	55916.091598	0.9469	1″	799.97	−134.8	−163.4	−48.75 ± 0.49	−339.79 ± 20.05
	21	55916.101421	0.0428	1″	799.96	−134.8	−169.6	−43.97 ± 0.44	−354.42 ± 15.82
	22	55916.111221	0.1384	1″	799.97	−134.8	−176.1	−41.06 ± 0.42	−255.63 ± 13.45
	23	55916.122672	0.2502	1″	799.96	−134.8	+176.6	−44.69 ± 0.46	−15.94 ± 18.30
	24	55916.132782	0.3490	1″	849.96	−134.8	+169.6	−46.23 ± 0.46	+153.76 ± 19.31
	25	55916.142895	0.4477	1″	799.96	−134.8	+163.1	−43.02 ± 0.46	+332.62 ± 18.44
	26	55916.154536	0.5613	1″	799.96	−134.8	+156.3	−41.91 ± 0.49	+285.43 ± 20.94
	27	55916.164373	0.6574	1″	799.97	−134.8	+151.1	−40.10 ± 0.48	+165.98 ± 18.92
	28	55916.174210	0.7534	1″	799.97	−134.8	+146.4	−39.74 ± 0.48	−54.07 ± 20.13

Continued on Next Page...

Table 1 – Continued

Target	No.	MJD_{bar}	ϕ	slit	exposure s	rotation deg	pos. angle deg	v_R ($km\,s^{-1}$)	v_{WD} ($km\,s^{-1}$)
	29	55916.229170	0.2900	1″	799.96	−134.8	+128.5	−12.85 ± 0.44	+89.37 ± 15.28
	30	55916.238967	0.3857	1″	799.97	−134.8	+126.5	−9.24 ± 0.43	+300.61 ± 17.14
	31	55916.250488	0.4982	1″	799.96	−134.8	+124.4	−9.52 ± 0.43	+350.95 ± 18.00
	32	55916.260274	0.5937	1″	799.97	−134.8	+122.8	−15.17 ± 0.55	+331.23 ± 22.73
	33	55916.270071	0.6894	1″	799.97	−134.8	+121.4	−18.58 ± 0.62	+89.53 ± 33.20
	34	55916.279869	0.7850	1″	799.97	−134.8	+120.2	−19.10 ± 0.76	−110.32 ± 50.99
	35	55915.181590	0.0641	2.″5	799.97	−134.8	+144.0		
	36	55916.190536	0.9148	2.″5	799.97	−134.8	+139.4		
EG 21	37	55915.031970		1″	21.99	0.0	−25.8		
	38	55915.034856		2.″5	21.99	0.0	−24.5		
HD 49798	39	55915.350264		1″	2.00	0.0	+72.6		
	40	55916.343776		1″	2.00	0.0	+71.3		
	41	55916.346515		2.″5	2.01	0.0	+72.3		
LTT 3218	42	55916.352238		2.″5	22.01	0.0	+58.8		
	43	55916.357062		2.″5	22.01	0.0	+62.4		
	44	55916.369131		1″	35.00	0.0	+64.5		
GD 108	45	55916.360948		2.″5	22.00	0.0	−176.4		
	46	55916.365961		1″	35.00	0.0	+179.9		

Table 2: Fractional binding energies of neutron stars (Data for Fig 4a).

Neutron Star	Mass ($M_\odot$)	Reference	Fractional Binding Energy
pulsars with white dwarf companions			
PSR J0348+0432	2.01	(this paper)	−0.1446
PSR J1141−6545	1.27	(*109*)	−0.0838
PSR J1738+0333	1.47	(*14*)	−0.0993
pulsars with neutron star companions			
PSR J0737−3039A	1.338	(*22*)	−0.0890
PSR J0737−3039B	1.249	(*22*)	−0.0822
PSR B1534+12	1.333	(*110*)	−0.0887
... companion	1.345	(*110*)	−0.0896
PSR B1913+16	1.440	(*111*)	−0.0969
... companion	1.389	(*111*)	−0.0929

Fractional binding energies of neutron stars in relativistic binaries, which are currently used in precision tests for gravity, and where the neutron star masses are determined with good (< few %) precision. The masses are taken from the given references. The specific numbers for the fractional binding energy are based on the equation-of-state ".20" of (*27*). A different equation-of-state gives different numbers, but does not change the fact that PSR J0348+0432 significantly exceeds the tested binding energy range.

References and Notes

1. J. H. Lattimer, M. Prakash, *Science* **304**, 536 (2004).
2. P. B. Demorest *et al.*, *Nature* **467**, 1081 (2010).
3. T. Damour, G. Esposito-Farèse, *Phys. Rev. Lett.* **70**, 2220 (1993).
4. T. Damour, G. Esposito-Farèse, *Phys. Rev. D* **54**, 1474 (1996).
5. C. M. Will, *Theory and Experiment in Gravitational Physics* (1993), Cambridge Univ. Press, Cambridge.
6. J. Boyles *et al.*, *ApJ* **763**, 80 (2013).
7. R. S. Lynch *et al.*, *ApJ* **763**, 81 (2013).
8. *Supporting Online Material*.
9. V. S. Dhillon *et al.*, *MNRAS* **378**, 825 (2007).

Table 3: Stellar envelope binding energies, $E_{\rm bind}$, for given donors and evolutionary stages.

Stage	$E_{\rm bind}$ (2.2 $M_\odot$)	$E_{\rm bind}$ (4.0 $M_\odot$)	CE outcome
$X_c = 0.40$	1.8×10^{49} erg	3.8×10^{49} erg	merger*
$X_c = 0.20$	1.6×10^{49} erg	3.4×10^{49} erg	merger*
$X_c = 0.02$	1.5×10^{49} erg	3.2×10^{49} erg	merger*
TAMS	1.6×10^{49} erg	3.6×10^{49} erg	may survive if $L_{\rm acc}$ can eject envelope
RGB	9.8×10^{47} erg	2.1×10^{48} erg	survives with $0.30 \leq M_{\rm WD}/M_\odot \leq 0.50$
AGB	2.0×10^{47} erg	1.9×10^{47} erg	survives with $0.44 \leq M_{\rm WD}/M_\odot \leq 0.72$

Envelope binding energies of stars with a total mass of 2.2 $M_\odot$ and 4.0 $M_\odot$, respectively. In all cases $E_{\rm bind}$ was calculated assuming $M_{\rm core} = M_{\rm WD} = 0.17\,M_\odot$, except for the cases where the RLO was initiated at the tip of the RGB/AGB with resulting values of $M_{\rm WD}$ as listed in the table.

* Note, that intermediate-mass donor stars on the main sequence ($X_c > 0$) with $P_{\rm b} > 1$ day, or at the TAMS, may avoid the onset of a CE altogether and evolve as a stable intermediate mass X-ray binary, IMXB (*112*).

10. M. van Kerkwijk, C. G. Bassa, B. A. Jacoby, P. G. Jonker, in *Binary Radio Pulsars*, F. Rasio, I. H. Stairs, eds., vol. 328 of *Astronomical Society of the Pacific Conference Series* (San Francisco, 2005), p. 357.

11. A. M. Serenelli *et al.*, *MNRAS*, **325**, 607 (2001).

12. J. A. Panei, L. G. Althaus, X. Chen, Z. Han, *MNRAS* **382**, 779 (2007).

13. M. Kilic, W. R. Brown, C. Allende Prieto, S. J. Kenyon, J. A. Panei, *ApJ* **716**, 122 (2010).

14. J. Antoniadis *et al.*, *MNRAS* **423**, 3316 (2012).

15. B. A. Jacoby, A. Hotan, M. Bailes, S. Ord, S. R. Kulkarni, *ApJ* **629**, L113 (2005).

16. B. Paxton *et al.*, *ApJS* **192**, 3 (2011).

17. F. Özel, *et al.*, *ApJ* **727**, L199 (2010).

18. A. Dowd, W. Sisk, J. Hagen, *Pulsar Astronomy - 2000 and Beyond, IAU Colloquium 177*, M. Kramer, N. Wex, R. Wielebinski, eds. (2000), vol. 202 of *Astronomical Society of the Pacific*, pp. 275–276.

19. T. Damour, J. H. Taylor, *Phys. Rev. D* **45**, 1840 (1992).

20. T. Damour, "Binary Systems as Test-beds of Gravity Theories", in *Physics of Relativistic Objects in Compact Binaries: From Birth to Coalescence*, M. Colpi, P. Casella, V. Gorini, U. Moschella, A. Possenti, eds., Astrophysics and Space Science Library, Volume 359, pp. 1-41 (Springer Netherlands, 2009).

21. I. H. Stairs, *Living Reviews in Relativity* **6** (2003), http://www.livingreviews.org/lrr-2003-5

22. M. Kramer *et al.*, *Science* **314**, 97 (2006).

23. P. C. C. Freire *et al.*, *MNRAS* **423**, 3328 (2012).

24. C. M. Will, *Living Reviews in Relativity* **9** (2006), http://www.livingreviews.org/lrr-2006-3

25. Y. Fujii, K.-I. Maeda, *The Scalar-Tensor Theory of Gravitation* (Cambridge University Press, 2003).

26. H. Goenner, *General Relativity and Gravitation* **44**, 2077 (2012).

27. M. Haensel, M. Kutschera, M. Prószyński, *A&A* **102**, 299 (1981).

28. P. C. C. Freire *et al.*, *ApJ* **675**, 670 (2008).

29. M. H. van Kerkwijk, R. P. Breton, S. R. Kulkarni, *ApJ* **728**, 95 (2011).

30. R. W. Romani *et al.*, *ApJ* **760**, L36 (2012).

31. J. Alsing, E. Berti, C. M. Will, H. Zaglauer, *Phys. Rev. D* **85**, 064041 (2012).

32. http://www.ligo.org/

33. https://wwwcascina.virgo.infn.it/

34. B. S. Sathyaprakash, B. F. Schutz, *Living Rev. Relativity* 12, (2009), http://www.livingreviews.org/lrr-2009-2

35. L. Blanchet, *Living Reviews in Relativity* **9** (2006), http://www.livingreviews.org/lrr-2006-4

36. C. M. Will, "Inaugural Article: On the unreasonable effectiveness of the post-Newtonian approximation in gravitational physics", *Proceedings of the National Academy of Science*, **108**, 5938 (2011)

37. M. Maggiore, " Gravitational Waves. Volume 1: Theory and experiments", *Oxford University Press* (2008).

38. Will, C. M., *Phys. Rev. D* **50**, 6058 (1994).

39. T. Damour, G. Esposito-Farèse, *Phys. Rev. D* **58**, 1 (1998).

40. I. Jr. Iben, M. Livio, *PASP* **105**, 1373 (1993).

41. T. M. Tauris, N. Langer, M. Kramer, *MNRAS* **416**, 2130 (2011).

42. T. M. Tauris, G. J. Savonije, *A&A* **350**, 928 (1999).

43. P. Podsiadlowski, S. Rappaport, E. D. Pfahl, *ApJ* **565**, 1107, (2002).

44. A. S. Fruchter, J. E. Gunn, T. R. Lauer, A. Dressler, *Nature* **334**, 686 (1988).

45. R. P. Breton, M. S. E. Roberts, S. M. Ransom *et al.*, *ApJ* **661**, 1073 (2007).

46. R. A. Chevalier, *ApJ* **411**, L33 (1993).

47. E. Pylyser, G. J. Savonije, *A&A* **208**, 52 (1989).

48. M. V. van der Sluys, F. Verbunt, O. R. Pols, *A&A* **440**, 973 (2005).

49. T. M. Tauris, N. Langer, M. Kramer, *MNRAS* **425**, 1601 (2012).

50. T. M. Tauris, *Science* **335**, 561 (2012).

51. M. Bailes *et al.*, *Science* **333**, 1717 (2011).

52. L. M. van Haaften, G. Nelemans, R. Voss, P. G. Jonker, *A&A* **541**, A22 (2012).

53. C. D. Dermer, A. Atoyan, *ApJ* **643**, L13 (2006).

54. D. Koester, *arXiv:0812.0482* (2008).

55. P.-E. Tremblay, P. Bergeron, *ApJ* **696**, 1755 (2009).

56. D. F. Gray, *The Observation and Analysis of Stellar Photospheres* (Cambridge University Press, 2005).

57. C. Kim, V. Kalogera, D. R. Lorimer, T. White, *ApJ* **616**, 1109 (2004).

58. D. J. Nice, I. H. Stairs, L. E. Kasian, *40 Years of Pulsars: Millisecond Pulsars, Magnetars and More*, C. Bassa, Z. Wang, A. Cumming, V. M. Kaspi, eds. (2008), vol. 983 of *American Institute of Physics Conference Series*, pp. 453–458.

59. G. B. Hobbs, R. T. Edwards, R. N. Manchester, *MNRAS* **369**, 655 (2006).

60. W. M. Folkner, J. G. Williams, D. H. Boggs, *Interplanetary Network Progress Report* **178**, C1 (2009).

61. C. Lange *et al.*, *MNRAS* **326**, 274 (2001).

62. D. Hobbs *et al.*, in *Relativity in Fundamental Astronomy: Dynamics, Reference Frames, and Data Analysis, IAU Symposium 261*, S. A. Klioner, P. K. Seidelmann, M. H. Soffel, eds. (Cambridge University Press, 2010), pp. 315–319.

63. I. Appenzeller *et al.*, *The Messenger* **94**, 1 (1998).

64. S. Bagnulo *et al.*, *The Messenger* **114**, 10 (2003).

65. P.-E. Tremblay, H.-G. Ludwig, M. Steffen, P. Bergeron, B. Freytag, *A&A* **531**, L19 (2011).

66. P. E. Tremblay, H. G. Ludwig, M. Steffen, B. Freytag, *ArXiv: 1302.2013*, (2013).

67. N. D'Amico *et al.*, *MNRAS* **297**, 28 (1998).

68. J. D. R. Steinfadt, L. Bildsten, P. Arras, *ApJ* **718**, 441 (2010).

69. A. M. Serenelli, L. G. Althaus, R. D. Rohrmann, O. G. Benvenuto, *MNRAS* **337**, 1091 (2002).

70. L. Henyey, M. S. Vardya, P. Bodenheimer, *ApJ* **142**, 841 (1965).

71. A. A. Thoul, J. N. Bahcall, A. Loeb, *ApJ* **421**, 828 (1994).

72. I. Iben, Jr., J. MacDonald, *ApJ* **296**, 540 (1985).

73. A. S. Eddington, *The Internal Constitution of the Stars* (Cambridge University Press, 1926).

74. J. J. Hermes, M. Kilic, W. R. Brown, M. H. Montgomery, D. E. Winget, *ApJ* **749**, 42 (2012).

75. M. H. van Kerkwijk *et al. ApJ* **715**, 51 (2010)

76. J. J. Hermes *et al.*, *ApJ* **750**, L28 (2012).

77. J. J. Hermes *et al. arXiv:1211.1022* (2012)

78. J. H. Applegate, *Astrophys. J.* **385**, 621 (1992).

79. A. H. Córsico, A. D. Romero, L. G. Althaus, J. J. Hermes, *arXiv:1209.5107* (2012).

80. D. J. Schlegel, D. P. Finkbeiner, M. Davis, *ApJ* **500**, 525 (1998).

81. J. M. Cordes, T. J. W. Lazio, *arXiv: 0207156* (2002).

82. D. R. Lorimer, M. Kramer. *Handbook of Pulsar Astronomy* (2004).

83. J. H. Taylor, *Philosophical Transactions of the Royal Society of London, A* **341**, 117 (1992).

84. T. Damour, N. Deruelle, *Ann. Inst. H. Poincaré (Physique Théorique)* **43**, 107 (1985).

85. T. Damour, N. Deruelle, *Ann. Inst. H. Poincaré (Physique Théorique)* **44**, 263 (1986).

86. B. Bertotti, L. Iess, P. Tortora, *Nature* **425**, 374 (2003).

87. P. C. C. Freire, N. Wex, *MNRAS* **409**, 199 (2010).

88. K. Lazaridis *et al.*, *MNRAS* **414**, 3134 (2011).

89. I. S. Shklovskii, *Soviet Ast.* **13**, 562 (1970).

90. T. Damour, G. W. Gibbons, J. H. Taylor, *Phys. Rev. Lett.* **61**, 1151 (1988).

91. T. Damour, J. H. Taylor, *ApJ* **366**, 501 (1991).

92. K. Nordtvedt, *Phys. Rev. Lett.* **65**, 953 (1990).

93. The effect of a variable gravitational constant on the orbital period decay $\dot{P}_{\rm b}$ of PSR J0348+0432 is actually mitigated by the change of the binding energy of the neutron star related to $\dot{G}$ (*92*). Since this change is both EOS and gravity theory dependent, we keep the more conservative expression of (*90*), which is anyway two orders of magnitude below our measurement precision of $\dot{P}_{\rm b}$.

94. F. Hofmann, J. Müller, L. Biskupek, *A&A* **522**, L5 (2010).

95. L. Motz, *ApJ* **115**, 562 (1952).

96. C. G. Bassa, M. H. van Kerkwijk, D. Koester, F. Verbunt, *A&A* **456**, 295 (2006).

97. T. Damour, G. Esposito-Farèse, *Class. Quantum Grav.* **9**, 2093 (1992).

98. K. Lazaridis *et al.*, *MNRAS* **400**, 805 (2009).

99. B. Paczynski, in *Structure and Evolution of Close Binary Systems, IAU Symposium 73*, P. Eggleton, S. Mitton, J. Whelan, eds. (Springer, 1976), p. 75.

100. R. E. Taam, E. L. Sandquist, *ARA&A* **38**, 113 (2000).

101. R. F. Webbink, *Astrophys. J.* **277**, 355 (1984).

102. M. Ugliano, H.-T. Janka, A. Marek, A. Arcones, *ApJ* **757**, 69 (2012).

103. N. Ivanova, *ApJ* **730**, 76 (2011).

104. S. Wellstein, N. Langer, *A&A* **350**, 148 (1999).

105. D. Bhattacharya, E. P. J. van den Heuvel, *Phys. Rep.*, **203**, 1 (1991).

106. P. C. C. Freire, *et al.*, *MNRAS*, **412**, 2763 (2011).

107. W. H. G. Lewin, M. van der Klis, Compact stellar X-ray sources, *Cambridge University Press* (2006).

108. R. N. Manchester, G. B. Hobbs, A. Teoh, M. Hobbs, *AJ*, 129, 1993 (2005), http://www.atnf.csiro.au/research/pulsar/psrcat/

109. N. D. R. Bhat, M. Bailes, J. P. W. Verbiest, *Phys. Rev. D* **77**, 124017 (2008).

110. I. H. Stairs, S. E. Thorsett, J. H. Taylor, A. Wolszczan, *ApJ* **581**, 501 (2002).

111. J. M. Weisberg, D. J. Nice, J. H. Taylor, *ApJ* **722**, 1030 (2010).

112. T. M. Tauris, E. P. J. van den Heuvel, G. J. Savonije, *ApJ* **530**, L93 (2000).

. J.A. is a member of the International Max-Planck research school for Astronomy and Astrophysics at the Universities of Bonn and Cologne. P.C.C.F. and J.P.W.V. gratefully acknowledge financial support by the European Research Council for the ERC Starting Grant BEACON under contract no. 279702. M.A.M. acknowledges support from a WVEPSCoR Research Challenge Grant. J.W.T.H. is a Veni Fellow of the Netherlands Foundation for Scientific Research. V.M.K. holds the Lorne Trottier Chair in Astrophysics and Cosmology, and a Canada Research Chair, a Killam Research Fellowship, and acknowledges additional support from an NSERC Discovery Grant, from FQRNT via le Centre de Recherche Astrophysique du Québec and the Canadian Institute for Advanced Research. MHvK and IHS acknowledge support from NSERC Discovery Grants. VSD, TRM and ULTRACAM are supported by the STFC. This work is based on data collected with the VLT of ESO under programme 088.D-0138A and observations with the 100-m Effelsberg telescope of the MPIfR. The Arecibo Observatory is operated by SRI International under a cooperative agreement with the National Science Foundation (AST-1100968), and in alliance with Ana G. Méndez-Universidad Metropolitana, and the Universities Space Research Association. The National Radio Astronomy Observatory is a facility of the National Science Foundation operated under cooperative agreement by Associated Universities, Inc. We are grateful to Detlev Koester and Jorge Panei *et al.* for providing models presented in their publications. We are obliged to Jonathan Smoker (ESO) for his help during the VLT observations and David Champion for assistance with the Effelsberg observations and useful discussions. We also thank Duncan Lorimer, Jocelyn Bell-Burnell, Giles Esposito-Farèse, Evan Keane, Philipp Podsiadlowski and Bernard Schutz for helpful discussions. This research has made use of NASA's Astrophysics Data System and Dr. Michael Thomas Flanagan's Java Scientific Library (www.ee.ucl.ac.uk/~mflanaga).